INTERNATIONAL JOURNAL FOR NUMERICAL METHODS IN FLUIDS, VOL. 8, 769 802 (1988)

NON-LINEAR TRANSIENT PHENOMENA IN A COMPLEX RECIRCULATING FLOW: A NUMERICAL INVESTIGATION

CHRISTOPHER J. FREITAS*

Southwest Research Institute, 6220 Culebra Rd, P.O. Drawer 28510, San Antonio, TX 78284, U.S.A.

AND

ROBERT L. STREET

Environmental Fluid Mechanics Laboratory, Department of Civil Engineering, Stanford University, Stanford, CA 94305-2179, U.S.A.

SUMMARY

A role of numerical methods in engineering research is illustrated in the present work, namely the use of computer algorithms as experimental facilities. A complex recirculating flow in a three-dimensional cavity was simulated and an extensive data base was generated which complements data measured in concurrent physical experiments. The objective of this numerical investigation was to improve understanding of physical phenomena in recirculating flows. The dominant physical phenomena in this shear-driven flow simulation are Taylor–Görtler vortices. These structures are intimately coupled with the primary recirculating flow and the effects of end-wall viscous damping.

KEY WORDS Three-dimensional cavity flow Incompressible flow Taylor–Görtler vortices Secondary flows

1. INTRODUCTION

The shear-driven cavity flow, a classic recirculating flow, is an idealization of many environmental, geophysical and industrial flows. In general these flows are characterized as possessing the following features: zones of recirculation or dominant eddies of the size of the flow domain; secondary motions induced by large-scale or turbulent phenomena; unsteady or transient flow conditions; and buoyancy-induced motions of various length scales. Often the complex dynamics present in this class of flows is not sufficiently understood to be modelled effectively and therefore to permit predictive computer algorithms.[1,2] Thus there is strong motivation to build a foundation in physical fundamentals and corresponding mathematical models. The cavity flow possesses all the relevant phenomena described above and allows for their analysis singly or in combination, permitting a systematic approach to understanding complex recirculating flows. The cavity flow problem in either its two- or three-dimensional form is an ideal vehicle for studying complex flow physics in a simple geometry.

The geometric simplicity and well defined flow structure in two dimensions and at low Reynolds numbers (Re) have allowed for comparative analysis of several numerical techniques in

* Formerly at Environmental Fluids Mechanics Laboratory, Stanford University.

0271 2091/88/070769–34$17.00

Received 17 December 1986
Revised 1 September 1987

the context of the cavity flow. Generally these two-dimensional, low-Reynolds-number ($Re \leqslant 400$) solutions are in good agreement. De Vahl Davis and Mallinson[3] and Tuann and Olson[4] reviewed these results. However, two-dimensional simulations of the cavity flow for $Re > 400$ have been less successful owing to the increased complexity of the flow and the inaccuracy of the numerical techniques employed. Most of these discretization schemes have used central differencing for the convective terms, which was believed to be numerically unstable for cell Reynolds numbers greater than two,[5] or stable HYBRID differencing,[6] which introduces spurious numerical diffusion owing to its first-order accuracy. These numerical inadequacies have been overcome and successful moderate-Reynolds-number, two-dimensional cavity flow simulations have been performed. These simulated flows are discussed in Ghia *et al.*,[7] who used a multigrid solution technique with fine nodal resolution, and Freitas,[8] who used a QUICK-type convective difference scheme of third-order accuracy.

Experimental results for moderate-Reynolds-number, three-dimensional shear-driven cavity flow indicate that the physics of this flow is anything but simple.[9-11] The flow field is highly unsteady and possesses significant secondary motions in the third or spanwise direction. The application of the often used assumption of two-dimensionality to the three-dimensional cavity flow is not generally valid.[3,12] The best two-dimensional simulations cannot reproduce the experimental velocity profiles and flow structure variation.[12] The discrepancies between these cavity solutions and the observed three-dimensional flow result from the absence of a mechanism for energy redistribution in the spanwise direction.[12,13]

Prior to the work reported in Freitas *et al.*,[13] three-dimensional simulations of the shear-driven cavity flow had not reproduced these observed flow patterns. Insufficient numerical accuracy seems to have been the principal cause of the lack of success of these simulations.[8] As indicated in Koseff *et al.*,[14] only the most general features of the three-dimensional cavity flow have been replicated. However, the numerical accuracy problem was overcome and preliminary results, verified by experimental data, for a moderate-Reynolds-number, three-dimensional shear-driven cavity flow were presented by the authors in Freitas *et al.*[12,13] This paper completes the analysis of the flow structure and physics of this cavity flow as reproduced by numerical simulations with the code REMIXCS. Details of the REMIXCS code and its advanced QUICK-type differencing scheme, as well as the cavity geometry and simulation conditions, are presented in Section 2.

The remaining sections of this paper present and discuss the flow features of a constant-density-fluid cavity flow at $Re = 3200$ (defined in Section 2). In general this complex flow is established and controlled by three phenomena. First, a primary recirculating flow exists due to the shear-induced motion of the fluid near the belt. This phenomenon dominates the early stages of the developing flow, i.e. the initial 2-3 min, and establishes the conditions which lead to the occurrence of the remaining two phenomena. Second, a pressure-driven secondary flow is generated and maintained by the interaction of the primary recirculating flow and the effect of end-wall viscous damping. This secondary flow establishes a spanwise cellular pattern in the half-cavity. The third phenomenon, Taylor Görtler vortices, develop due also to interactions between the primary recirculating flow and the kinetic energy sink effect of the end-wall. The Taylor Görtler (TG) vortices subsequently modify the primary recirculating and pressure-driven secondary flows.

The flow structure at a time 20 min after the belt was instantaneously set in motion is recorded in Section 3. Figures 2-8 present a detailed view of this fully developed flow. Section 4 examines TG phenomena in terms of spatial development and their influence on the global flow structure. Again the 20 min velocity field is used in this analysis. Transient aspects of this flow and TG temporal dynamics are analysed in Section 5. Finally a summary of results for this series of simulations and the study's conclusions are given in Section 6.

2. REMIXCS, CAVITY DEFINITIONS AND SIMULATION CONDITIONS

2.1. *REMIXCS code*

A complete description of the REMIXCS code REcirculating MIXed Convection Simulator) is presented in Freitas *et al.*[13] and Freitas.[8] A brief review of the main features of this code is given here for completeness. REMIXCS is based on the REBUFFS code, developed by J. A. C. Humphrey of the University of California, Berkeley.[15] Both codes are derivatives of the group of TEACH codes developed at Imperial College, London, by Gosman and Pun[16] and whose fundamentals were conceived by Patankar and Spalding.[17] REMIXCS solves a weak form of the Navier–Stokes equations in primitive variables via a weighted-residual method. The difference equations are derived by volume integration of the partial differential equations on a control volume surrounding each node of the computational grid. The weighting function is set equal to unity for the control volume over which integration has taken place and zero everywhere else. An advantage of this formulation is that quantities such as mass, momentum and energy are conserved over any group of control volumes and thereby over the entire computational domain.[6]

REMIXCS is structured on the SIMPLE algorithm.[6] This iterative procedure utilizes the concept of a pressure correction equation, i.e. a modified Poisson equation for pressure. A modification to the original solution method of REBUFFS for the pressure correction equation system has reduced the CPU time (for cases tested) by a factor of four and the number of iterations per time step by a factor of seven. The line-by-line tridiagonal solver for the pressure correction equation system in REMIXCS consists now of a bidirectional sweep. In past formulations, after a line-by-line solution traverse on a given x–y plane is completed, the process is repeated on the next x y plane, thus sweeping all planes in the z-direction. In the bidirectional sweep introduced in REMIXCS, after sweeping all x–y planes, the sweep direction is rotated to the y-axis and a line-by-line traverse on an x–z plane is performed. This accounts quite effectively for the elliptic nature of the pressure.

The convective terms in REMIXCS are differenced via a QUICK-type scheme. The development and implementation of this QUICK-type scheme is the most significant numerical modification in REMIXCS. QUICK (quadratic upstream interpolation for convective kinematics) was originally invented by Leonard[18] and subsequently studied in various forms by, among others, Han *et al.*,[19] Pollard and Siu,[20] Leschziner[21] and Paolucci and Chenoweth.[22] These formulations were all two-dimensional in structure and for uniform grid spacing. Negative aspects of these QUICK-type schemes were: excessive computational cost beyond that of the HYBRID scheme;[23] boundedness problems manifesting themselves by slight overshoots and undershoots;[21, 24] and stability problems.[19] In the QUICK-type scheme developed and implemented here, these inadequacies have been eliminated for two- and three-dimensional formulations and uniform and non-uniform node spacing. Implementation of the non-uniform grid version of this scheme, for example, increased execution times by only 39% above that of the original HYBRID formulation. In addition, stability of this QUICK-type method is similar to and has the operational limits of the HYBRID scheme, and boundedness problems did not occur. Details of this QUICK-type scheme are presented in Freitas *et al.*[13] and Freitas.[8]

2.2. *Cavity flow definitions*

This series of transient simulations studied a three-dimensional, shear-driven flow in a cavity for constant-property fluid (water) conditions. Geometric and general flow definitions are presented in Figure 1. The experimental cavity has a width B of 150 mm, a depth D of 150 mm

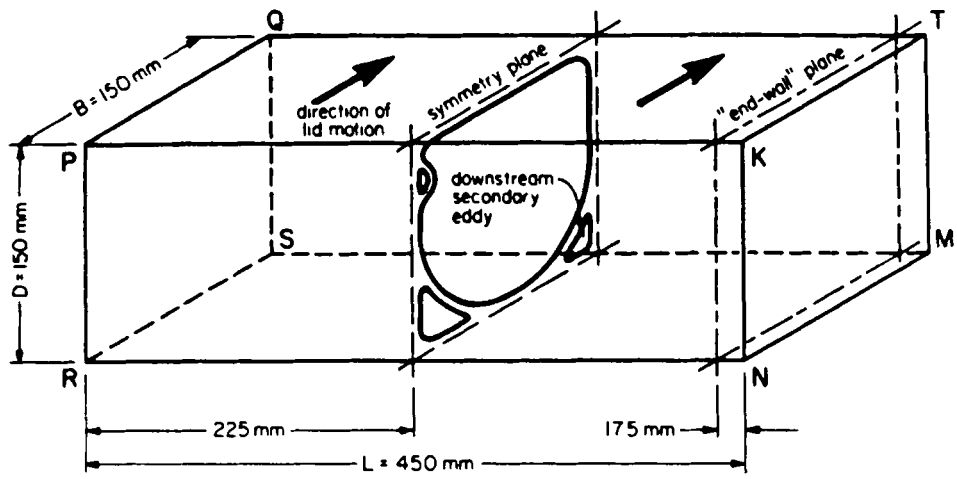

BOUNDARY DEFINITIONS

END-WALL : PQSR	SIDE-WALL UPSTREAM : PKNR
: KTMN	DOWNSTREAM : QTMS
LID : PQTK	LOWER HORIZ. : SMNR

Figure 1. Geometric and general flow definitions

and a lateral span L of 450 mm. This geometry results in a depth-to-width aspect ratio (D/B) of 1:1 and a span-to-width aspect ratio (L/B) of 3:1. The Reynolds number for this cavity is defined as $Re = U_b B/\nu$, where U_b is the belt speed and ν is the average kinematic viscosity of the working fluid, water. The belt speed for this study is 21·3 mm s^{-1} and the corresponding Re is 3200. Techniques employed in and results of the concurrent experimental investigation of this flow are discussed in Koseff[11] and Koseff and Street.[9, 10]

2.3. *Conditions of simulations*

The cavity flow was simulated on a non-uniform grid of $32 \times 32 \times 45$ for the half-cavity. Experimental results show a symmetric mean flow about the centre plane of the lateral span, and thus simulating the half-cavity flow only is a valid approximation. Additionally it is economically prudent. The numerical boundary condition imposed at the centre plane is that of a zero-flux surface with free-slip vertical and horizontal velocity conditions. The remaining five surfaces were represented by no-slip velocity boundary conditions. The transient simulation began with quiescent initial conditions and used variable time steps ($0{\cdot}02\ \text{s} \leqslant \Delta t \leqslant 10{\cdot}0\ \text{s}$) to generate the 25 min flow history. Grid nodes were distributed such that the nodes nearest the walls were 0·075 mm from the wall. On planes parallel to the symmetry plane (Figure 1) the grid resolution places seven nodes within 2·5 mm of the wall, eleven nodes within 10 mm of the wall and twelve nodes within 20 mm of the wall (see Figure 2). For planes parallel to the upstream wall the grid resolution places nine nodes within 6·5 mm of the end-wall and 15 nodes within 20 mm of the end-wall. The typical TG vortex pair is resolved by six to eight nodes. This grid resolution is sufficient because it resolved the measured length scales of fluid motion in the cavity.

Flow was initiated by instantaneously starting the belt at time zero. Experimental and numerical results indicate that the flow becomes fully developed in approximately 5 min. A true steady state does not exist for this flow, however; it continuously evolves in time. As is shown in this paper, the complex interaction of various scales of quasi-periodic motion control and establish a locally unsteady flow. A range of quasi-periodic time scales develop and are related to a full range of length scales, from those of the order of the cavity dimensions to those of the order of the TG vortices.

In general, a grid-based solution of the governing flow equations is only capable of resolving structures larger than twice the grid spacing (the minimum resolved wavelength). A three-dimensional grid-based solution implies a filtering process performed over a control volume in which scales of motion larger than the averaging volume are explicitly simulated, while the unresolved or sub-grid-scale (SGS) phenomena must be neglected or modelled. The mathematical spatial filtering process of the governing equations results in two groups of terms, namely those representing the spatial-averaged (or grid-averaged) dependent variable and those describing the SGS influence on the dependent variable. In this study we have performed direct numerical simulations because these SGS terms are neglected; no explicit model is used to represent the SGS influence on the resolved flow field. This simplification is justified only if all pertinent scales of motion are resolved on the discretized flow domain. However, QUICK-type schemes do introduce to the discretized equation set a local truncation error equivalent to fourth-order dissipation. This dissipation term can act as an 'implicit SGS model' in the direct numerical simulations and thereby dissipate the energy of the smallest resolved scales (the principal function of a SGS turbulence model). Thus this fourth-order numerical dissipation prevents energy from accumulating in the smallest resolved scales, which, if allowed to occur, can lead to numerical stability problems.[25]

These calculations were performed at the IBM Palo Alto Scientific Center (PASC) on an IBM-3081 computer running the VM operating system. Approximately 8 megabytes of core were required with real variables at double precision. Simulations using single-precision real words resulted in non-physical solutions and spurious wiggles in the dependent variable fields. Approximately 400 CPU hours were used to simulate 25 min of the flow, representing a non-dimensional time period of 213 (equal to the number of transits of a fluid particle along the cavity belt length) based on cavity width and belt speed.

3. DESCRIPTION OF FULLY DEVELOPED FLOW

This flow is established and maintained by the interaction among the primary recirculating flow, the pressure-driven secondary flow and the TG vortices. The primary recirculating flow is generated by the lid or belt dragging the adjacent fluid. The dragged fluid collides with the downstream vertical wall (see Figure 1) and is deflected downward. A secondary eddy is formed in the apex of the vertical and bottom boundaries as a result of frictional losses and stagnation pressure. Another secondary eddy is generated in the upstream lower corner, which is the response of the primary circulating fluid to the upstream vertical wall and the associated negative pressure gradient. A third secondary eddy may develop on the upstream vertical wall (see Figure 1) near the lid, its formation being dependent on the magnitude of the local velocity. This eddy occurs because, while the flow along the vertical upstream wall is responding to the approaching corner, as the flow on the other walls did, the lid is drawing fluid out of the corner in the lid boundary layer.

Figure 2 displays the structure of this primary recirculating flow at selected spanwise locations. Figure 2(a) displays these features through particle tracks on a plane 40 mm from the end-wall.

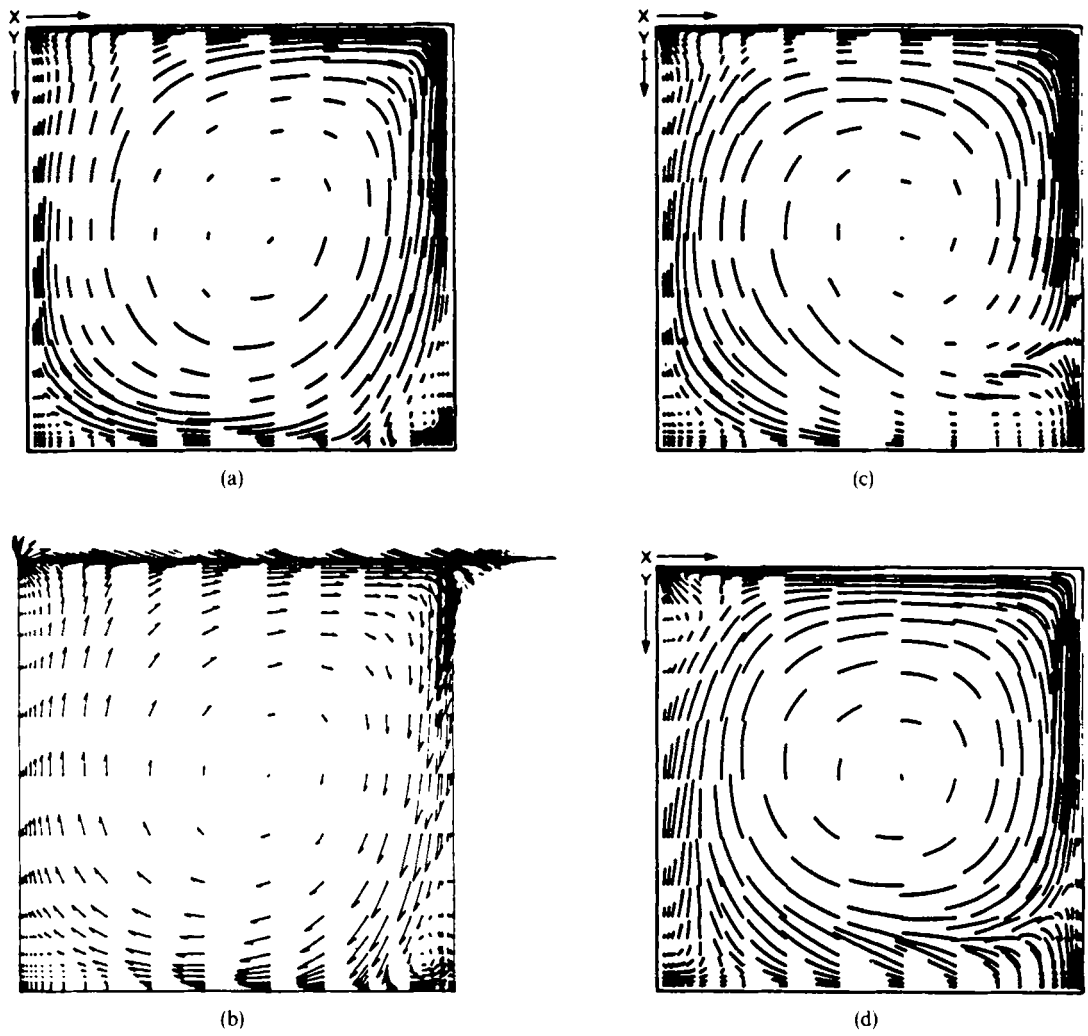

Figure 2. 4 s particle track and vector fields at selected spanwise locations. Velocity field at time = 20 min. (a) Particle track field on a plane 40 mm from end-wall. (b) Vector field on a plane 40 mm from end-wall. (c) Particle track field on a plane 10 mm from end-wall. (d) Particle track field on symmetry plane

The duration of particle motion is 4 s. In general particle tracks are generated by solving the system $\mathbf{dx}/dt = \mathbf{v}$ for an instantaneous velocity field $\mathbf{v}$, assumed constant during the duration of particle motion. Figure 2(b) presents the identical field as vectors normalized by the belt speed and indicates the direction of flow. An equivalent two-dimensional solution of lid-driven flow in a cavity at $Re = 3200$ possesses these same features.[8] However, further similarities between the two-dimensional simulation and the three-dimensional cavity flow are precluded by two conditions not present in a two-dimensional simulation of cavity flow. First, there is an end-wall. Second, the concave separation line separating the primary vortex from the downstream secondary eddy is now a surface subject to spanwise variation. As a result, the intensity and size of the primary vortex and secondary eddies become dependent on their spanwise location and time. This spanwise variation is recorded in Figures 2(c) and (d).

Spanwise variation in flow structure is not solely due to end-wall effects, but is a result of the complex interaction of spanwise pressure gradient, radial pressure gradient, centrifugal force and the no-slip velocity boundary condition. Due to these effects, an end-wall corner eddy (EWCE) is generated in the apex of the vertical end-wall and the bottom plate, and pairs of TG vortices develop. In addition, a tendency for a global pressure-driven secondary flow develops because of the presence of a spanwise pressure gradient from the end-wall to the symmetry plane, a result of viscous damping at the boundaries of the primary recirculating flow. Figure 3 displays this EWCE and the TG vortices. In order to enhance visualization of the flow structure on this plane, the primary circulation velocity has been filtered out and only motions in the spanwise plane are recorded. The viewpoint in this three-dimensional perspective view (and several subsequent figures) is from behind the corner created by the intersection of the upstream wall and the end-wall. The belt motion is indicated by the arrow and only the half-cavity is shown, i.e. from the end-wall to the symmetry plane. The EWCE and four pairs of variably sized TG vortices are clearly seen in Figure 3.

The TG vortices in Figure 3 develop along the concave separation surface that forms between the primary vortex and the downstream secondary eddy. In general, TG vortices result from the destabilizing influence of concave streamlines.[26] When fluid is constrained to turn a corner, centrifugal forces acting on the fluid are balanced by an increased radial pressure, producing a stable condition. This stable condition for curved streamlines can be described by a free or potential vortex, where velocity is proportional to the reciprocal of the radius. In the presence of a boundary layer (or boundary-layer-type velocity profile) the centrifugal force/radial pressure gradient equilibrium is disrupted by viscous effects. The centrifugal forces are reduced (below those of the potential vortex case) in the lower-velocity layers because of viscous and shear effects, and the associated pressures are weaker than those in an ideal fluid. In the free-stream, conditions are equivalent to the potential vortex or ideal flow condition. Thus a radial pressure gradient is set up from the free-stream to the boundary layer region. TG vortices occur then because of the sensitivity of this flow condition to small disturbances which are, in turn, propagated and amplified in the direction normal to the plane of the primary flow. TG vortices and related phenomena are reviewed by Freitas.[8]

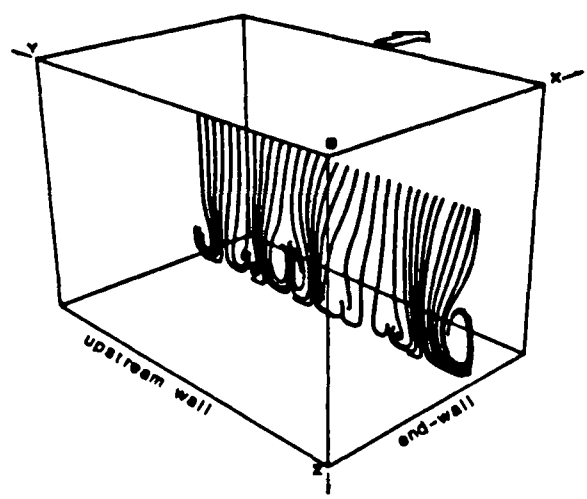

Figure 3. Particle track field on a plane 45 mm from downstream wall (wall QTMS in Figure 1). Duration of particle tracks = 60 s. Velocity field at time = 20 min

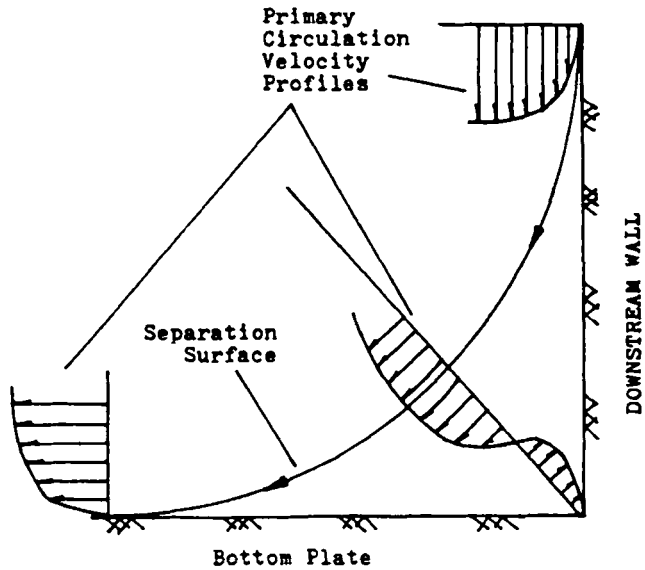

Figure 4. Schematic of radial velocity profile in the region of the downstream wall, bottom plate corner

Figure 4 presents the typical radial profile of tangential velocity that exists in the region of the downstream corner of the cavity. The separation surface is characterized by a boundary-layer-type profile with the velocity maximum marking the apparent location of the separation surface. A radial pressure gradient develops from the primary vortex flow region (free-stream-like flow) to the secondary flow region (wall-layer-like flow). Thus a particle radially displaced by centrifugal forces encounters insufficient pressure gradient to return it to its original position. Therefore the combination of centrifugal force/radial pressure gradient imbalance and a spanwise perturbation result in TG vortex formation. It is hypothesized here that in the cavity flow the primary 'trigger' mechanism which initiates TG vortex formation is end-wall viscous damping and EWCE effects. This hypothesis is discussed in Section 5.1, but briefly the EWCE induces a wave-like disturbance (due to its development and transient nature) which propagates from the end-wall and perturbs the centrifugal force/radial pressure gradient imbalance that exists along the concave separation surface. The complex interaction of centrifugal instability and the spanwise perturbation wave result in TG vortex formation.

Figure 3 demonstrates that the spanwise variation of flow observed in Figure 2 is a consequence of the presence of large-scale spanwise structures. The impact on the global flow due to the EWCE and TG vortices is readily seen in the following sequence of figures.

Figures 5(a) and (b) are different perspective views of the same particle tracks, with particles initially released near the bottom plate and approximately 15 mm from the downstream wall. These particles tend to move toward and up the downstream wall and then some are drawn out and into the primary flow, while others remain in the secondary eddy flow region. The path which a particle will follow is determined by the local velocity field, which is affected by the TG vortices and EWCE. In Figure 5(b) the EWCE and three pairs of TG vortices are represented by particle paths which traverse the cavity width. Significant spanwise motions in the downstream secondary eddy region are associated with these structures. In selected zones between these structures, closed circulation cells exist (Figure 5(a)).

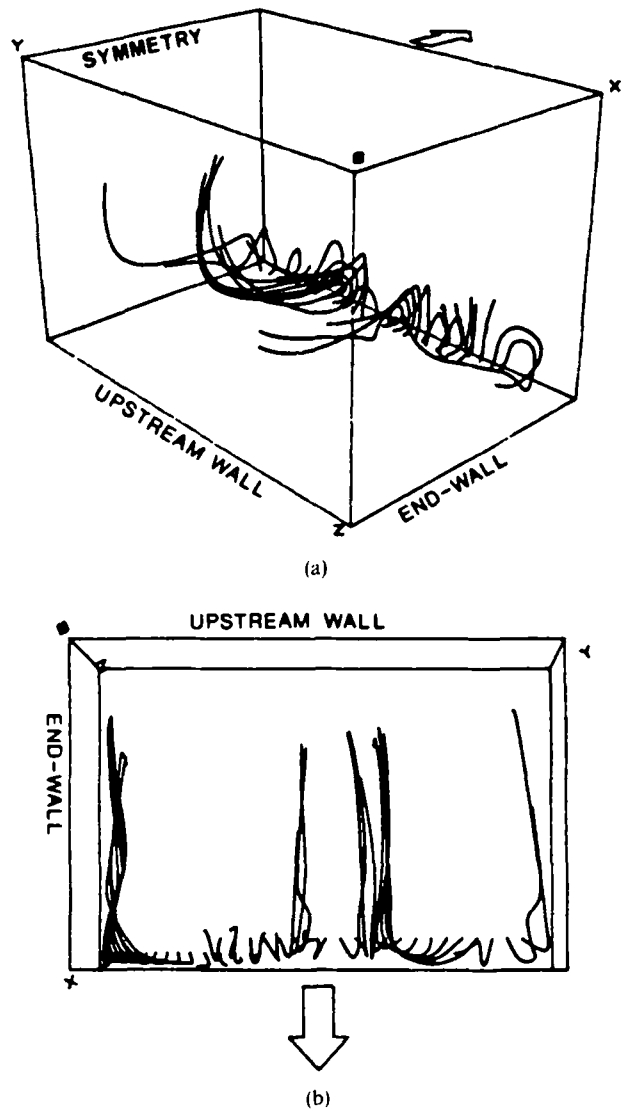

Figure 5. 60 s particle tracks, initially released near bottom plate and 15 mm from downstream wall. Velocity field at time = 20 min. (a) End-wall corner perspective view. (b) View from above cavity (looking down)

Figures 6(a) and (b) are similar perspective views of a different set of particle tracks in the vicinity of the downstream wall. These particles are released near the belt (or top of the cavity), approximately 15 mm from the downstream wall. The particles move in the direction of the belt toward and then down the downstream wall. Some particles are drawn into the primary circulation, while others again remain in the downstream secondary eddy flow. Those particles drawn into the primary circulation are associated with the flow in the TG vortices and EWCE.

These figures emphasize the following points:

(a) that a well defined (closed) downstream secondary eddy exists only between TG vortex pairs where strong spanwise motions are absent

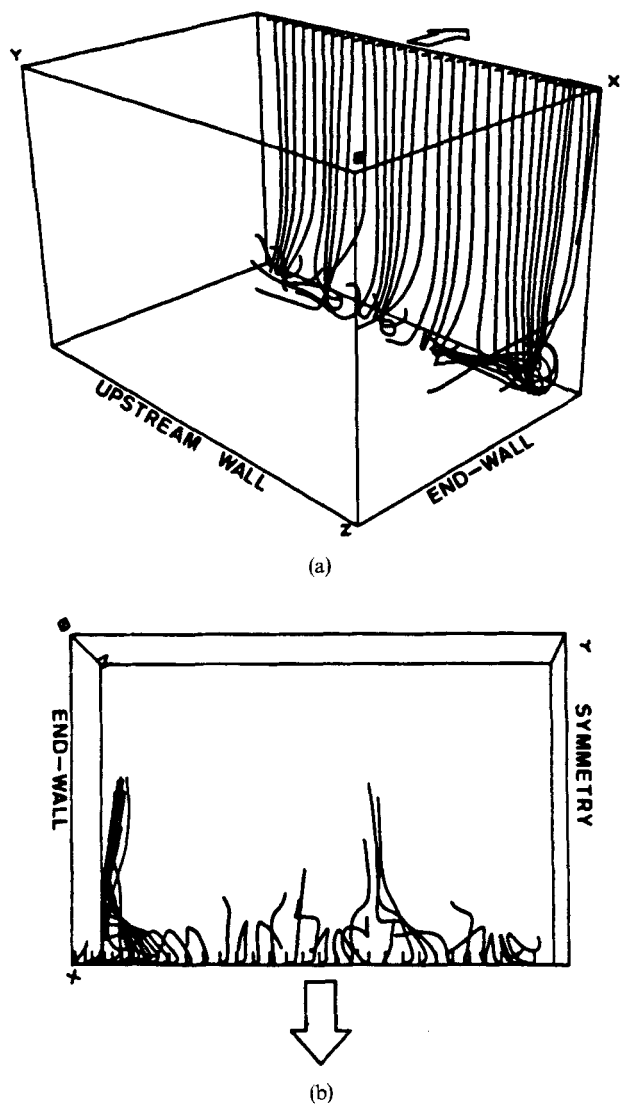

Figure 6. 60 s particle tracks, initially released near the belt and 15 mm from downstream wall. Velocity field at time = 20 min. (a) End-wall corner perspective view. (b) View from above cavity (looking down)

(b) that the EWCE and TG vortices induce significant spanwise motions near the downstream wall, disrupting the development of a closed secondary eddy
(c) the EWCE and TG vortices correspond to regions of high-velocity fluid, indicated by longer path lengths which extend across the cavity width.

In addition, particle paths become 'braided' within the EWCE and TG vortices, indicating that these are zones of longitudinal vorticity.

The flow structure in the vicinity of the upstream wall is examined in Figure 7. Particles are released in the boundary layer flow at the bottom of the cavity. The particles move toward the upstream wall. The key observation in this figure is that the flow field has become banded, with

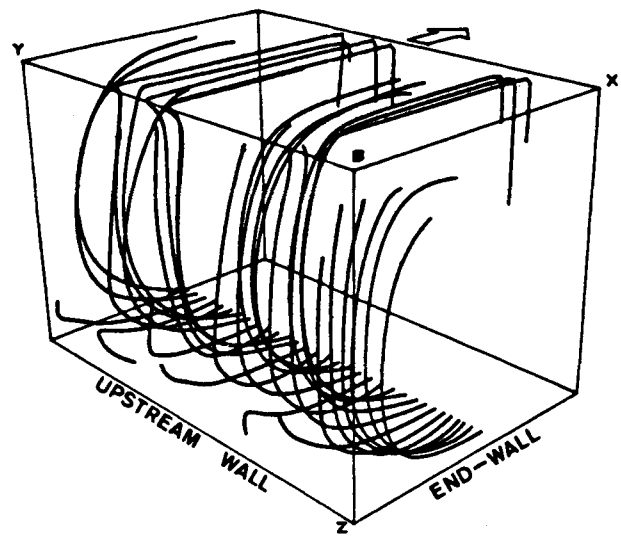

Figure 7. 60 s particle tracks, initially released 3 mm from bottom of cavity and on centreline of cavity width (75 mm from upstream wall). Velocity field at time = 20 min

alternating zones of low- and high-velocity fluid. The upstream secondary eddy is modified and spanwise motions are again present. The potential for a well defined upstream secondary eddy exists in regions between the upstream vertical wall and the concave surface formed by the reattaching high-velocity fluid. In general, the high-velocity fluid (corresponding to TG vortices) separates earlier than the low-velocity fluid and thus a well defined separation bubble or secondary eddy develops. Unlike the downstream wall phenomena, spanwise motions dominate low-velocity areas near the upstream secondary eddy and between TG vortex pairs, where fluid is drawn into the recirculating flow of the upstream secondary eddy. In general, flow in the vicinity of the upstream secondary eddy is less organized than flow in its downstream counterpart.

TG vortices do not appear to develop along the reattaching separation surface on the upstream wall. This may be due to the reduced velocity and larger radius of curvature associated with this surface (see Figure 2(a)) and thereby a stable condition may exist here. Görtler[27] found that at the onset of vortex motion a characteristic parameter, now known as the Görtler number (G), has a certain positive value which is related to the vortex wave number and the boundary layer thickness. Following Smith,[28] G is based on the boundary layer Reynolds number $Re_\delta\,(=U_\infty \delta/\nu)$, the boundary layer momentum thickness δ and the radius of curvature of the wall r_c, as follows:

$$G = Re_\delta^2 \delta / r_c$$

The wave number A is defined as $2\pi/\lambda$, where λ is the vortex wave length.

If we assume the radius of curvature to be $B/2$ ($=75$ mm), U_∞ to be 9 mm s^{-1} (based on the separation surface tangential velocity) and δ to be approximately 2 mm (a quarter of the boundary layer thickness), then G is approximately 8 for conditions at the downstream wall. This magnitude of G corresponds to the unstable region of the neutral stability curves[29] for all values of A. Therefore we would expect to see a range of possible wavelengths for this flow and, in fact, do. As presented in Sections 4 and 5, TG vortex wavelengths of 30–50 mm occur (wave numbers of 0·1–0·2 mm^{-1}). For conditions along the upstream wall separation surface, G is approximately 1–2 (based on $U_\infty = 4$ mm s^{-1} and $r_c = 100$ mm). This value of G approaches that for a stable

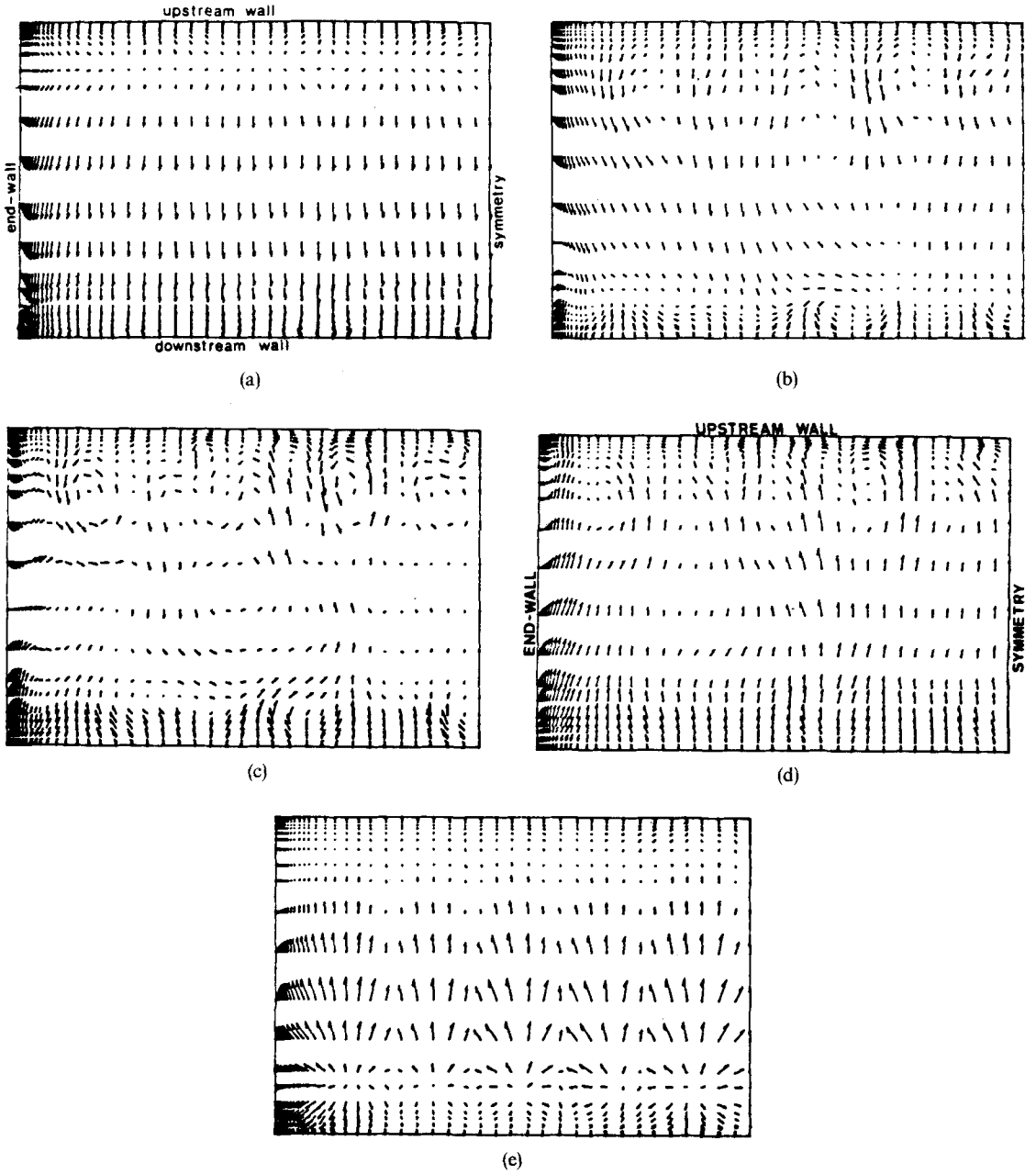

Figure 8. Vector fields on planes parallel to belt surface or top of cavity. Velocity field at time = 20 min. (a) Plane 10 mm below belt surface. (b) Plane 54 mm below belt surface. (c) Plane 75 mm below belt surface. (d) Plane 96 mm below belt surface. (e) Plane 145 mm below belt surface

condition and thus new TG vortices do not appear along this surface. However, TG vortices which were generated at the downstream wall may dominate the local flow on the reattaching surface at the upstream wall and may then be amplified further by its associated centrifugal instability.

Figure 8 completes the description of the fully developed instantaneous flow field at time 20 min. This series of figures presents vector fields in horizontal planes parallel to the belt or plane PQTK in Figure 1. Belt motion in these figures is from the upstream wall (top of figure) to the downstream wall (bottom of figure). Flow in Figures 8(a) and (e) is dominated by the boundary layer flow along the belt surface or cavity bottom respectively. Significant three-dimensional phenomena are present, though, in Figures 8(b), (c) and (d), and the influence of the TG vortices is readily observed on the downstream and upstream walls.

Figure 8 also records the presence of the end-wall boundary layer flow and some end-wall corner eddies. These features result from the interaction of the primary recirculating flow and end-wall viscous damping effects. In addition, Figures 8(b), (c) and (d) display colliding boundary layer flow along the end-wall. A wavy mixing layer, developing from the collision region at the end-wall to the core region of the cavity, is also observed. In Section 4.3 it is demonstrated that these flow phenomena are related to large-scale flow cells. As discussed in Section 1, these cells result from a pressure-driven secondary flow.

4. THE TAYLOR–GÖRTLER PHENOMENA

4.1. *Spatial development*

The EWCE and concave separation surface off the downstream wall are fundamental to the development of TG vortices. Figure 9 highlights the various stages in their spatial development through a series of particle tracks on sequentially spaced spanwise planes. As in Figure 3, visualization of the flow structure on these planes has been enhanced by filtering out the primary circulation velocity. Only motions in the spanwise planes are recorded.

The plane displayed in Figure 9(a) is 0·7 mm from the downstream wall. The influence of the EWCE on fluid near the downstream wall at the end-wall corner is evident. The line demarking the separation surface near the downstream wall, i.e. between regions of downflow (primary circulation) and upflow (secondary circulation), is also recorded. Two key observations in this figure are that the contour of the separation surface is irregular, and significant spanwise motions already exist near the downstream wall in the secondary circulation zone. These phenomena were also observed experimentally by Koseff.[11]

Figure 9(b) shows a plane approximately 5 mm from the downstream wall. The strength and zone of influence of the EWCE has increased. At the separation surface, particles are being swept in the spanwise direction by developing vortical structures. However, the pathlines above the separation surface are essentially straight and parallel, demonstrating that spanwise motions are generated at the separation surface and are not a result of flow irregularities above the separation surface.

Figure 9(c) shows a plane 11 mm from the downstream wall. Across the span, irregular penetration of the downward moving fluid is observed. This further indicates that the downstream secondary eddy is not likely to be uniform in size over the span length. In addition, several isolated vortical structures exist.

A plane 15 mm from the downstream wall is displayed in Figure 9(d). The EWCE is fully developed and, as a result, a small TG vortex pair begins to develop immediately adjacent to it. Along the span, more developing TG pairs are apparent. The non-linearity of the development phenomenon of TG vortices is evident in this figure in that a variable distribution and size of counter-rotating vortices exist. If this phenomenon were linear, then we should observe a spanwise decay of the EWCE effect due to viscous damping. In the remaining figures, i.e. Figures 9(e) and (f), the TG vortices continue to develop and increase in size and strength.

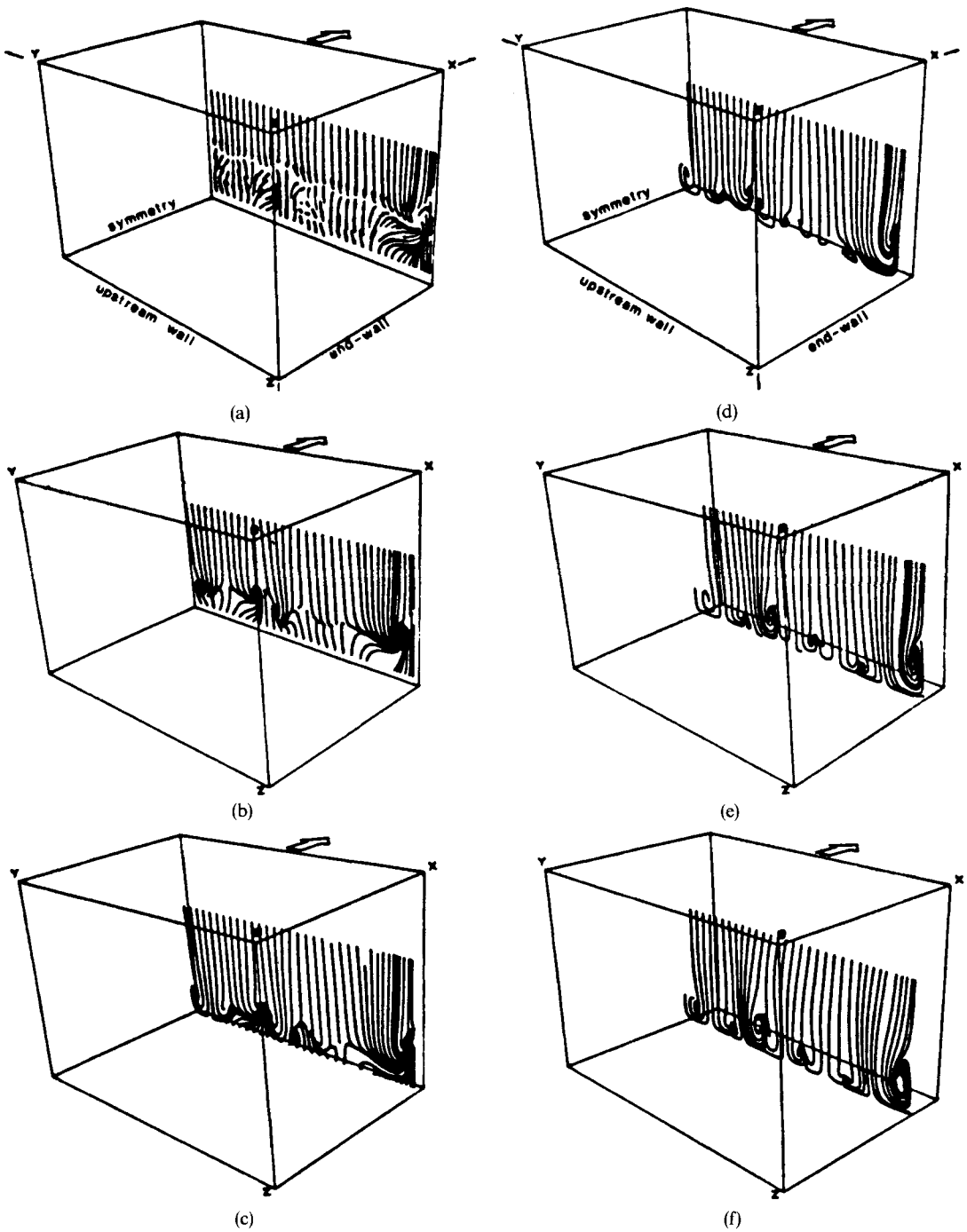

Figure 9. Spatial development of TG vortices. 60 s particle tracks based on 20 min instantaneous velocity field. End-wall corner perspective view. (a) Particle track field on a plane 0·7 mm from downstream wall. (b) Particle track field on a plane 5 mm from downstream wall. (c) Particle track field on a plane 11 mm from downstream wall. (d) Particle track field on a plane 15 mm from downstream wall. (e) Particle track field on a plane 23 mm from downstream wall. (f) Particle track field on a plane 30 mm from downstream wall

Several conclusions can be drawn from Figure 9. First, TG vortices develop variably along the span. This is indicative of the second-order instability associated with the non-linear amplification of the centrifugal force/radial pressure gradient imbalance. A uniform spatial development of the TG vortices would be driven by a first-order or primary instability of the force imbalance and its non-linear amplification.[30] Second, TG vortex development is related to the development of the EWCE. Third, all spanwise structures increase in size in the streamwise flow direction. However, as discussed in Section 3, the presence of the upstream wall inhibits continued development of TG vortices. Therefore, Wortmann's[30] third-order instability of TG vortices does not appear to develop in this cavity flow. Fourth, there are no disturbances upstream of the separation surface (on the downstream wall) to affect TG formation. Finally, the local effect of TG vortices on the downstream secondary eddy structure is to introduce a flow component parallel to the downstream wall and to modify the eddy's spanwise structure (as indicated in Section 3).

4.2. *TG modification of velocity profiles*

A quantitative indicator of the three-dimensional character of this flow and a further indication of the local effect of TG vortices on the primary recirculating flow is presented in Figure 10. Centreline profiles of the vertical velocity component (normalized by the belt speed) at three span locations, namely at a plane between TG pairs, at a plane bisecting a TG vortex pair and at a plane bisecting a single vortex of a TG pair, are displayed in Figure 10(a). At the downstream wall QTMS ($x/B = 1{\cdot}0$) TG vortices tend to reduce the magnitude of the vertical velocity by redistributing energy into the spanwise direction. The effect is greatest at planes which bisect a single vortex. The velocity gradient at the boundary and the boundary layer thickness, however, are only slightly modified by the presence of the vortices on the downstream wall. The boundary layer thickness in all three profiles is about 8 mm, but the maximum velocity varies by about 30%.

At the upstream wall ($x/B = 0{\cdot}0$) TG vortices significantly reduce the velocity gradients at the wall and shift the maximum-velocity point further from the wall. As demonstrated in Figure 9, TG vortices are fully developed before reaching the upstream wall. Therefore, once fully developed, TG vortices appear to effectively diffuse momentum and vorticity from the vicinity of the bottom and upstream walls, and thereby modify the velocity profiles. This is further evident in Figure 10(b).

Figure 10(b) shows the corresponding centreline normalized profiles of the horizontal velocity. At a plane between TG vortices a sharp velocity gradient exists at the cavity bottom. At planes in which TG vortices are present the vortices smooth these gradients through diffusion or transport of momentum from the near-wall region into the primary vortex. The inflection (at $y/D = -0{\cdot}85$) in the two profiles affected by the vortices occurs at the level of the core of the corresponding TG vortex.

Figure 10 displays the strength of the primary circulation at selected planes and thereby demonstrates that the major effect of TG vortices is to redistribute energy from the primary flow direction into a direction normal to the primary flow. TG structures transport high-momentum fluid from the near-wall regions at a rate greater than the laminar boundary layer would, thus producing a boundary layer profile similar in shape to that of a turbulent flow. Winoto and Crane[31] have measured similar variations in velocity profiles due to the presence of Görtler vortices in curved channel flow.

An estimate of the percentage of the total kinetic energy which is redistributed from the two-dimensional primary flow into spanwise motions can be computed. The total kinetic energy in the half-cavity is the summation (over the half-cavity volume) of the local kinetic energy associated with each control volume of the computational grid, i.e. the total kinetic energy equals

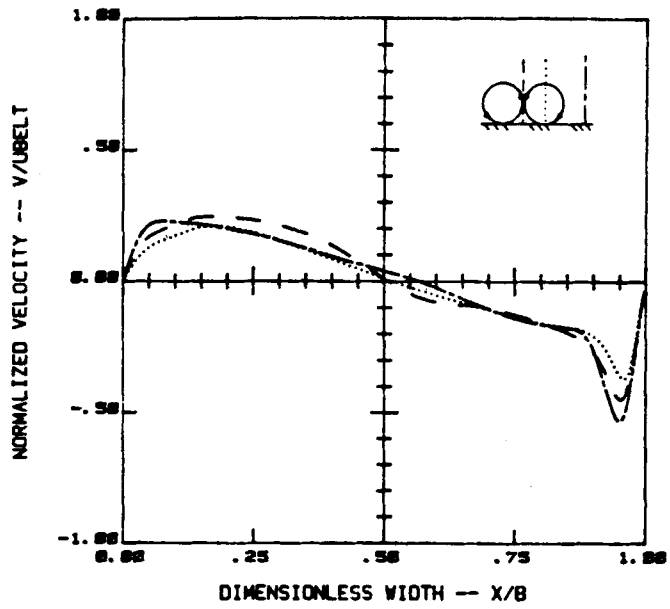

(a)

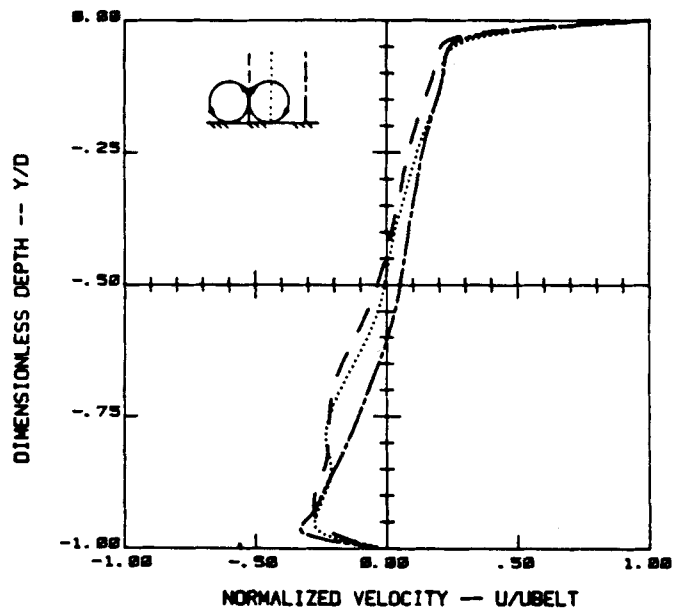

(b)

Figure 10. Centreline profile of velocity at various span locations; bisecting TG vortex pair (– –), bisecting TG vortex (. . . . .), and between TG vortex pairs (–·–). The co-ordinates of each plane are irrelevant since the TG vortices meander in time. (a) Vertical normalized velocity profiles. (b) Horizontal normalized velocity profiles

$\Sigma(\rho/2)(u^2+v^2+w^2)\ V_{cv}$. This sum is $5{\cdot}13\times10^{-5}\,\mathrm{kg\,m^2\,s^{-2}}$ and is distributed among the kinetic energy of each velocity component, with 49% of the total kinetic energy in the vertical velocity field, 50% in the horizontal velocity field and 1% in the spanwise velocity field. The kinetic energy associated with the spanwise velocity field is the result of large-scale effects on the flow by the end-wall and smaller-scale effects of the TG vortices.

Locally TG vortices redistribute approximately 1% of the kinetic energy associated with a thin slice (parallel to the end-wall) of the flow. This was determined by computing the kinetic energy on each of the planes in Figure 10. These planes possess approximately the same amount of kinetic energy. On the plane between TG vortex pairs, where minimum spanwise motions occur, 0·25% of the local kinetic energy is associated with the spanwise velocity field. Thus TG vortices may account for a fourfold increase in the local kinetic energy associated with the spanwise velocity field. This small amount of kinetic energy (in the spanwise velocity field) belies the impact that TG vortices and end-wall effects have on establishing this shear-driven cavity flow.

An effective method for evaluating the ability of a two-dimensional simulation to reproduce the equivalent spanwise average three-dimensional velocity field is to compare two-dimensional velocity profiles with three-dimensional profiles averaged over the spanwise axis. The spanwise average of the three-dimensional field accounts for variation in flow structure across the span and produces a profile which is representative of the equivalent two-dimensional flow. Figure 11 displays this comparison. Here the three-dimensional span-averaged normalized vertical and horizontal velocity profiles (neglecting the end-wall region) are plotted with the equivalent two-dimensional simulation results.[8] Also included in these figures are the physical experimental data. The experimental data points represent 256 sample averages of velocities measured by laser-Doppler anemometry on the symmetry plane of the equivalent physical flow.[11]

It is obvious in this figure that the two-dimensional simulation overestimates the total kinetic energy of the flow. Thus, if a two-dimensional simulation is used to model the effective mixing within a three-dimensional cavity, then some mechanism for energy redistribution or dissipation must be incorporated in the governing equations. In general, a two-dimensional simulation is incapable of resolving the flow physics within a three-dimensional cavity. Of course, the three-dimensionality of such a flow is dependent on the cavity span-to-width aspect ratio and the Reynolds number of the flow. Therefore conditions may exist where the span-to-width aspect ratio is sufficiently large and the Reynolds number sufficiently small to make a two-dimensional simulation of flow in a cavity valid.

Agreement between the span-averaged three-dimensional velocity profiles and measured velocity profiles in Figure 11 is quite good. In essence, the instantaneous span-averaged profiles are equivalent to the time-averaged effect that occurs at the symmetry plane in the experiments as the TG vortices meander across the symmetry plane with a period of approximately 80 s.[11] The zero-flux boundary condition imposed at the symmetry plane inadvertently fixes a single TG vortex at this plane (refer to Figures 3 and 9) and thus modifies the computed time-averaged profile. However, in the span-averaged process similar realizations of velocity field modification as in the physical experiments are achieved, producing similar velocity profiles.

4.3. *Impact of TG vortices on global flow—single-particle tracks*

De Vahl Davis and Mallinson[3] presented a single-particle track descriptive of the general motion of fluid in the primary vortex for a three-dimensional cavity flow (spanwise aspect ratio of 2:1) at $Re = 100$. The velocity field was steady for this Reynolds number and cavity geometry. The particle was released near one end-wall, close to the centre of the primary vortex. It spiralled toward the symmetry plane of the cavity where the particle gradually progressed outward and

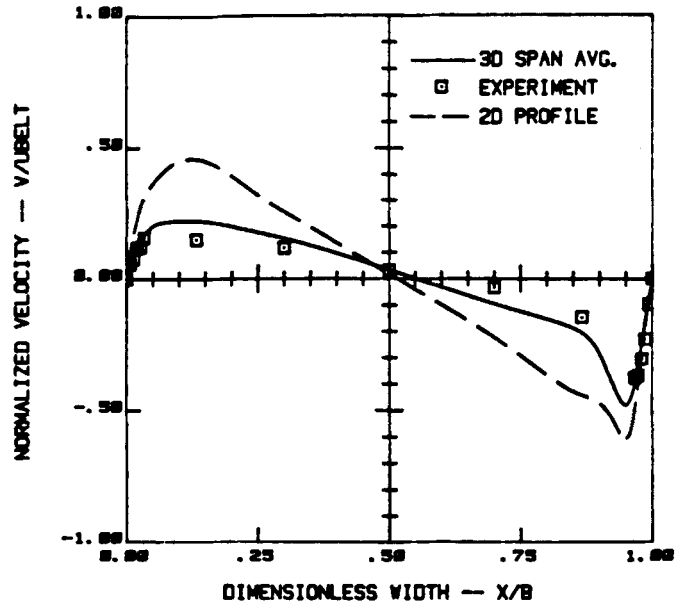

(a)

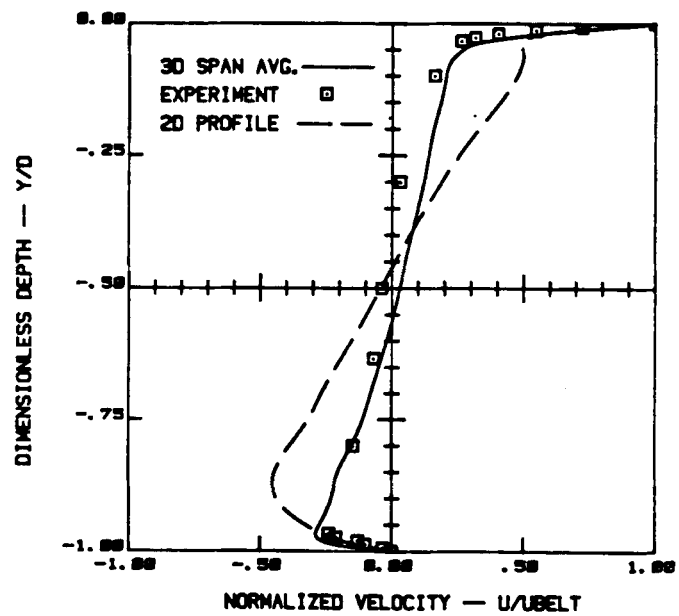

(b)

Figure 11. Comparison of centreline velocity profiles from experiment, 2D simulation and span-averaged 3D simulation. Fully developed flow in both computations and experiments. (a) Vertical normalized velocity profile comparison. (b) Horizontal normalized velocity profile comparison

returned to the end-wall region via the boundary layer. Figures 12–16 use a similar technique to investigate the motion of fluid in the primary vortex for our flow case at $Re = 3200$. This is accomplished through two perspective views each of five different single-particle tracks. The 20 min instantaneous velocity field is used in the computation of particle paths. The duration of each particle motion varied from 1000 to 1200 s. Therefore a true picture of the unsteady flow is not represented in these figures, but they do give a general picture of the large-scale cell structure in the cavity.

In Figure 12 the particle, having been released in a region of flow with large angular velocity, migrates in large loops toward the end-wall. There the particle motion is modified by the interaction of the end-wall boundary layer, pressure gradients and EWCE. These effects force the particle to spiral inward. A spanwise pressure gradient (from the end-wall to the symmetry plane) then drives the particle in the direction of the symmetry plane through small-radial loops. Eventually this particle stops its spanwise translation and continues to rotate in a closed loop within the primary vortex at a fixed span location. The spanwise translation of this particle is interrupted by the presence of a TG vortex at this location (refer to Figures 5 and 6).

Figure 13 records the history of a particle released at approximately the final span location of the particle in Figure 12. Again this particle is driven by large angular velocity and rotates in large-radial loops moving slowly toward the end-wall. The downstream and upstream walls' boundary layers drive this migration (refer to Figure 8). Eventually this particle is drawn into the EWCE flow and begins to retrace the path of the particle in Figure 12. This particle's path is determined by the cumulative effects of the boundary layer flows at the walls and the irregular large-scale flow, modified across the span by TG vortices.

The influence on the flow of the free-slip, zero-flux numerical boundary condition at the symmetry plane and of the resulting stationary TG vortex is again recorded in Figure 14. This particle tends to remain in the boundary layers along the rigid surfaces, rotating in large loops. The particle does meander from the symmetry plane into the core flow, but then closes the circulation cycle by returning to the symmetry plane via the boundary layers. The motion of this particle is controlled by the fixed TG vortex at the symmetry plane.

The core flow of the primary vortex is recorded in Figures 15 and 16. The particle in Figure 15 meanders through the centre of the primary vortex from the end-wall to the symmetry plane, driven by the spanwise pressure gradient. Figures 12, 13 and 15 demonstrate that a general circulation pattern exists which is toward the end-wall via the boundary layer regions on the downstream and upstream walls and toward the symmetry plane in the central core flow. This was observed experimentally and is reported by Koseff.[11] This pattern is also similar to that observed by De Vahl Davis and Mallinson[3] for $Re = 100$. Figure 16 demonstrates, however, that locally there is a central core flow from the symmetry plane toward the end-wall. The particle in this figure is released near the symmetry plane and meanders slowly toward the end-wall, but stagnates when it encounters the core flow of Figure 15. Where this confluence of core flows occurs also corresponds to the location of the largest TG vortex pair, as displayed in Figures 9, 5 and 6.

In this cavity flow TG vortices disrupt the general circulation observed by De Vahl Davis and Mallinson[3] for $Re = 100$ where TG vortices are not present. Instead, TG vortices modify the pressure-driven secondary flow to create a large spanwise cellular flow consisting of counter-rotating structures. In the end-wall cell region, flow is toward the end-wall via the boundary layers and toward the symmetry plane in the core. In the symmetry plane cell region, flow is toward the symmetry plane via the boundary layers and toward the end-wall in the core. These flow trends are also seen in Figure 8. Therefore the predicted global flow structure for this cavity and at a Reynolds number of 3200 consists of four counter-rotating spanwise flow cells in the half-cavity.

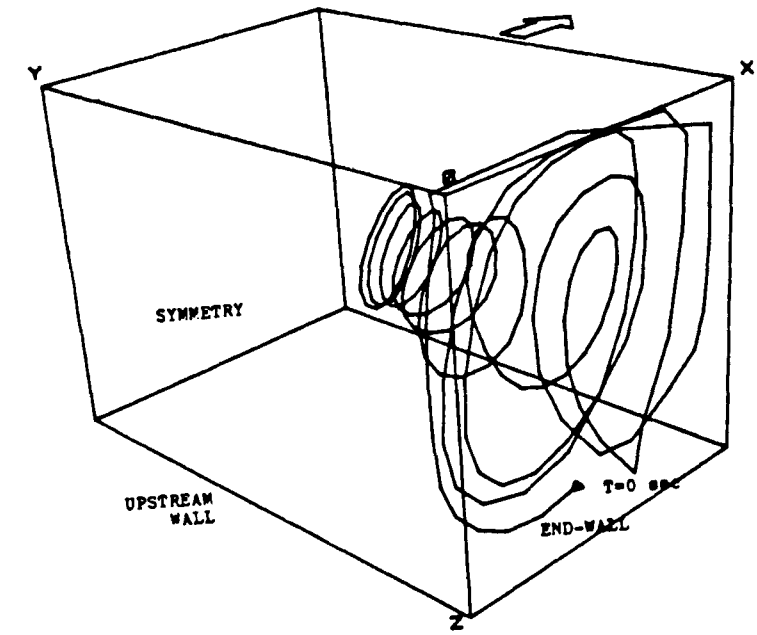

(a)

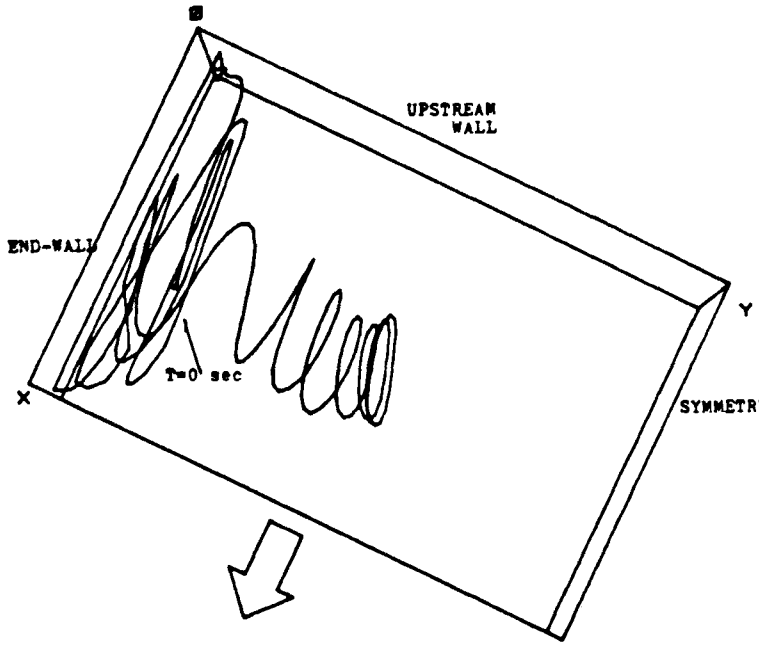

(b)

Figure 12. Single particle released 3 mm from cavity bottom and 25 mm from end-wall. (a) End-wall corner perspective view. (b) View from above cavity (looking down)

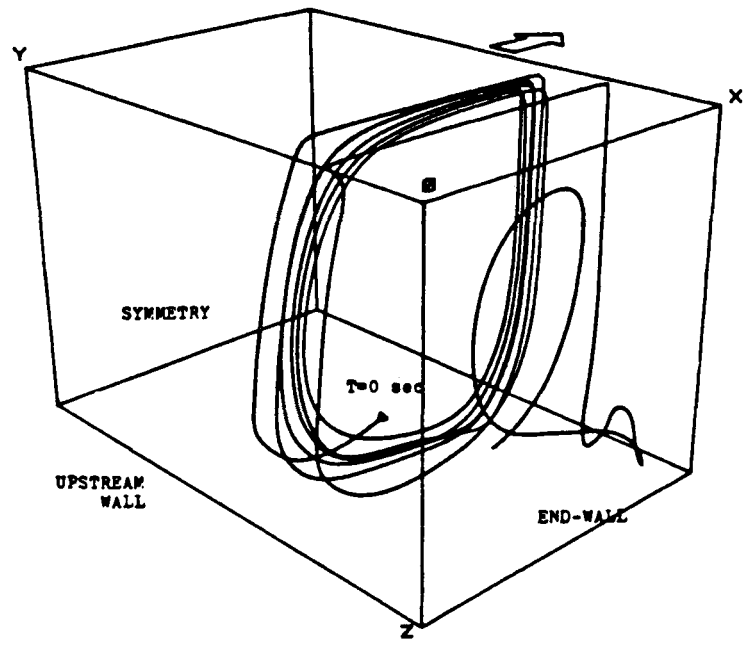

(a)

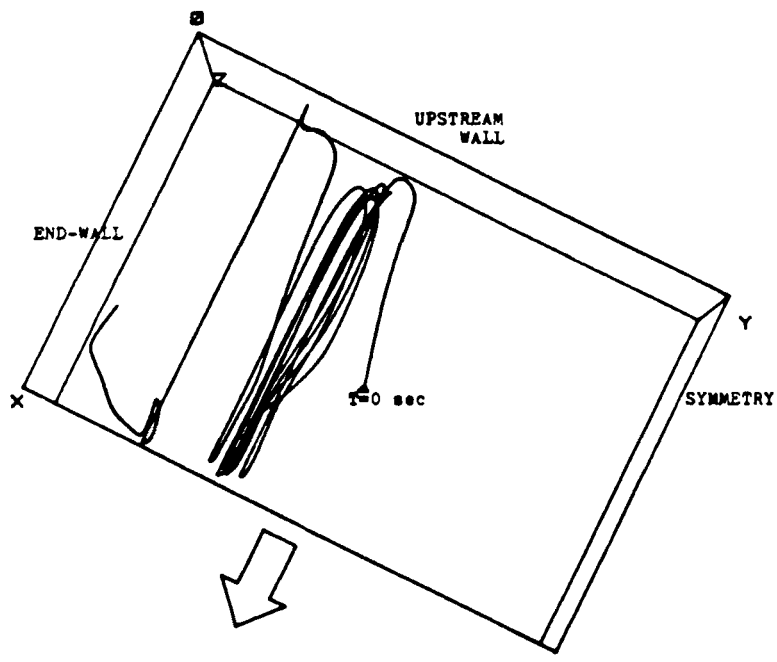

(b)

Figure 13. Single particle released 3 mm from cavity bottom and 112 mm from end-wall. (a) End-wall corner perspective view. (b) View from above cavity (looking down)

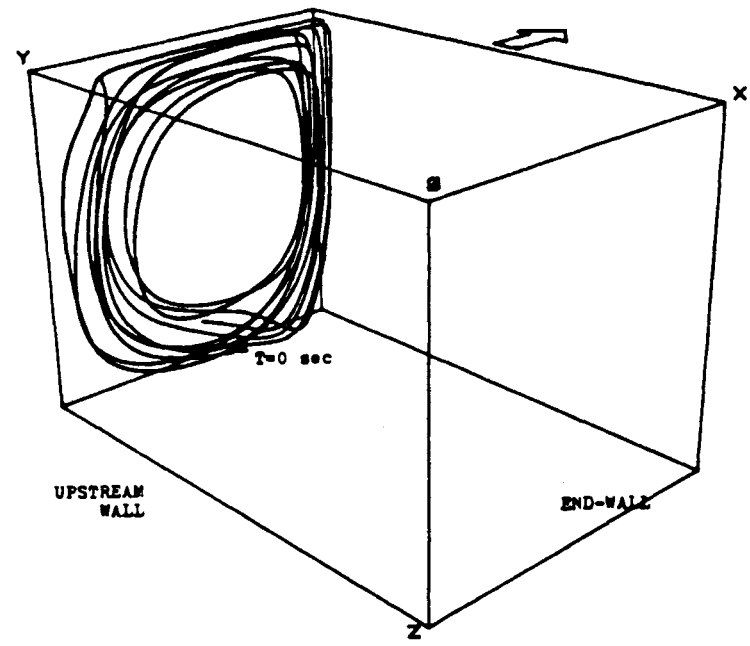

(a)

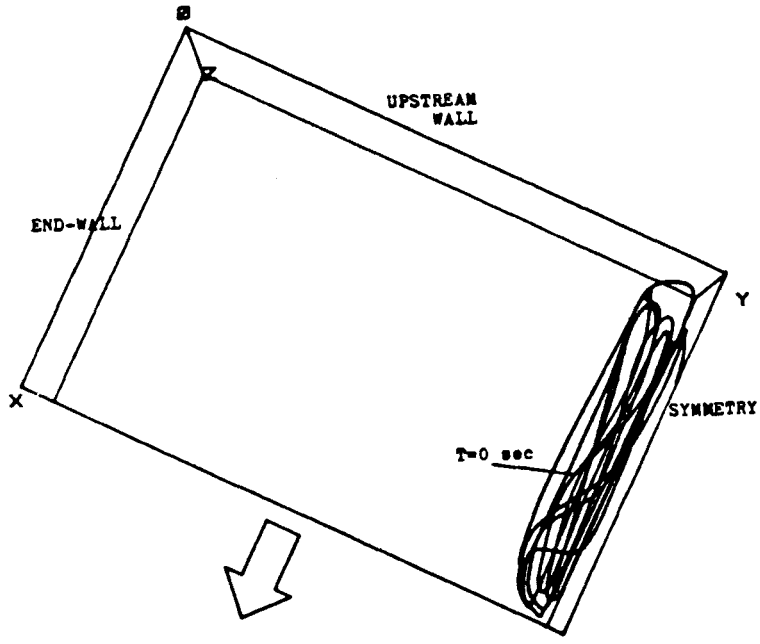

(b)

Figure 14. Single particle released 3 mm from cavity bottom and near the symmetry plane (220 mm from end-wall). (a) End-wall corner perspective view. (b) View from above cavity (looking down)

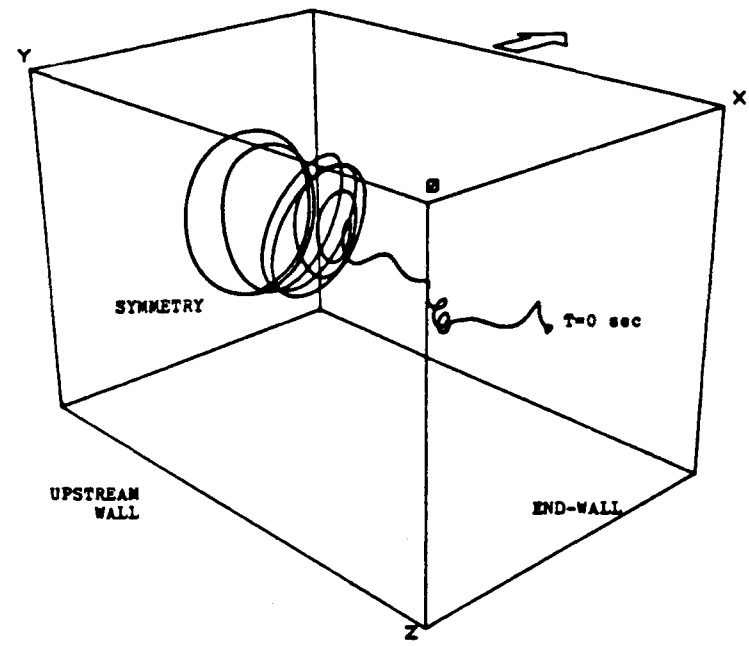

(a)

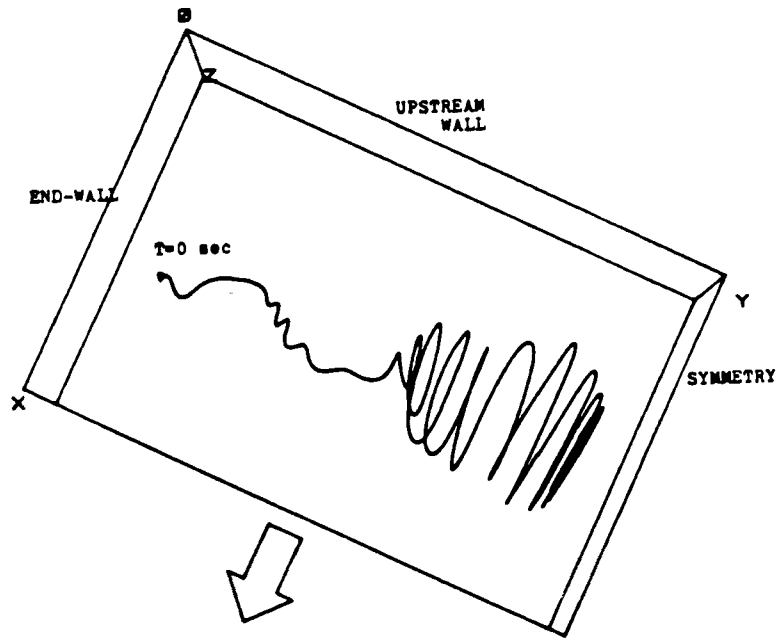

(b)

Figure 15. Single particle released at centre of primary vortex and 25 mm from end-wall. (a) End-wall corner perspective view. (b) View from above cavity (looking down)

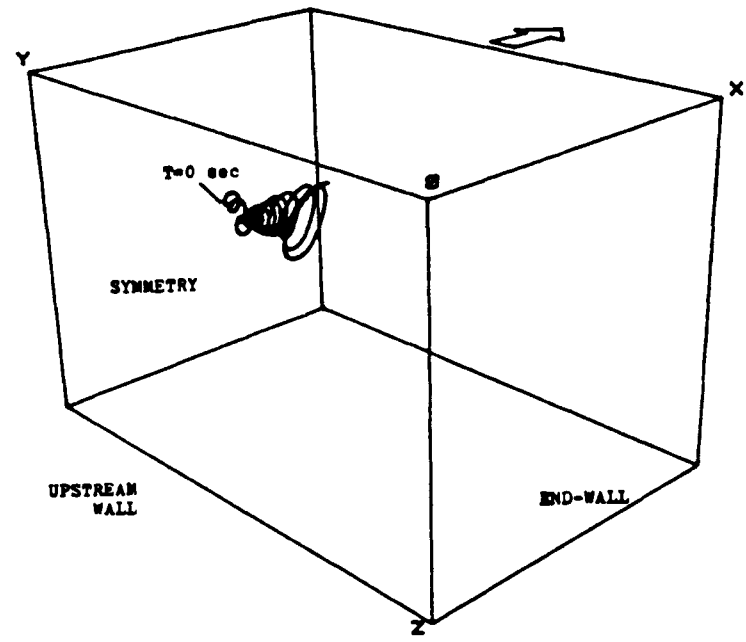

(a)

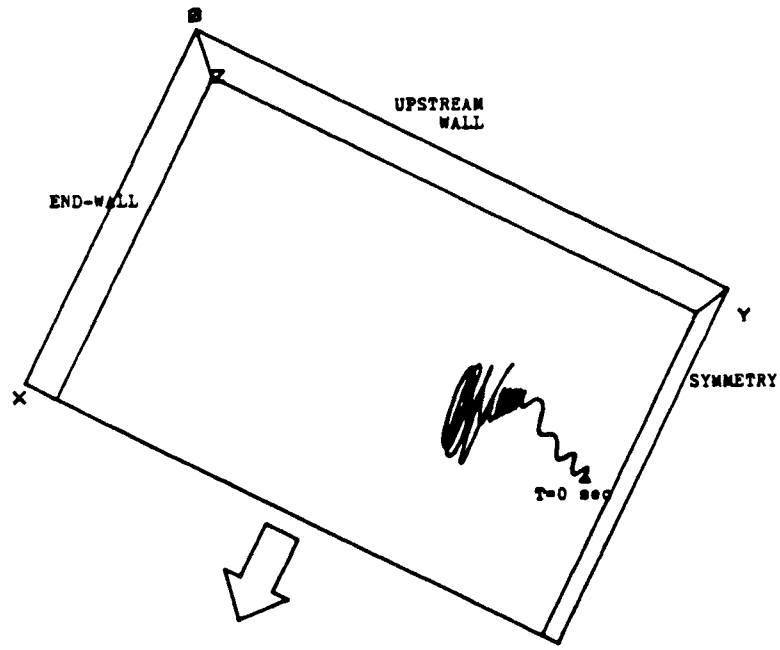

(b)

Figure 16. Single particle released at centre of primary vortex and near the symmetry plane (220 mm from end-wall). (a) End-wall corner perspective view. (b) View from above cavity (looking down)

5. TAYLOR–GÖRTLER DYNAMICS

5.1. *End-wall 'trigger' hypothesis*

The hypothesis of an end-wall 'trigger' mechanism for development of TG vortices in this flow is predicated on two observations. First, TG vortex formation occurs 2–3 min after initiation of belt motion for $Re = 3200$ (in both physical experiment and numerical simulation). This period is equivalent to the time required for the EWCE to develop. Second, numerical simulations of laterally unbounded curved boundary layer flow, e.g. Winoto and Crane,[31] or numerical simulations of three-dimensional slices of the cavity flow, e.g. Kim and Moin,[32] or physical experimental investigations of laterally unbounded curved boundary layer flow, e.g. Aihara,[33] must all be artificially perturbed to stimulate TG vortex development.

In general, TG vortex formation requires two distinct and necessary components. The first component, as discussed previously, is the curved separation surface with its associated centrifugal force/radial pressure gradient imbalance. The second necessary component is a spanwise perturbation which is amplified by the centrifugal force/radial pressure gradient imbalance. This spanwise perturbation in the cavity results from the no-slip boundary condition at the end-wall. It establishes a spanwise pressure gradient, an end-wall boundary layer and the EWCE. The spanwise perturbation which is naturally created by end-wall effects here is artificially reproduced by the random spanwise disturbance which investigators often superimpose on a steady flow in order to generate Görtler vortices.

A further indication of the significance of the end-wall perturbation and EWCE on TG vortex formation can be found in Koseff *et al.*[14] The three-dimensional half-cavity simulation discussed there used HYBRID differencing on a $23 \times 23 \times 23$ non-uniform grid for $Re = 2000$. The EWCE was reproduced, but the experimentally observed TG vortices were not. The failure to resolve the TG vortices in this simulation was not due to insufficient resolution as proposed by the authors, because as shown in Freitas[8] an equivalent $21 \times 21 \times 24$ non-uniform grid with the QUICK-type scheme does resolve TG vortices. Rather, it is proposed that the failure of this former simulation to resolve TG vortices is due to the excessive numerical damping of the upwind component of the HYBRID scheme. This numerical viscosity damps the end-wall perturbation and the diffusion of energy from the primary flow to the spanwise or secondary flow and thereby inhibits vortex formation. The QUICK-type scheme, however, transmits the end-wall perturbation into the flow field and the transfer of energy from the primary to secondary flow because of its lack of artificial diffusion. Thus TG vortices are predicted on grids with the QUICK-type scheme for which first-order schemes do not predict TG vortex formation.

5.2. *Time history of flow at a plane*

The complex dynamics of TG vortices is examined next, through a time sequence of vector plots on a plane 35 mm from the downstream wall QTMS. A time interval of 3 min was simulated with time steps of 1 s beginning with the 20 min velocity field, which represents a fully developed flow. Figure 17 shows the evolution of the flow field during this period in the form of vector plots every 20 s. Only the lower third of the cavity depth is displayed in Figure 17. In this region the primary flow is moving away from the reader.

The initial observation in Figure 17 is that TG vortices vary significantly in pair size, in time and in space. Also the pairs are asymmetric. This phenomenon corresponds to Wortmann's[30] second mode instability. The lifetime or time scale of any TG pair is dependent to some degree on its length scale, i.e. a large length scale correlates with a longer time scale. For example, the large TG pair (approximately 150 mm from the end-wall) has a wavelength of about 50 mm and a time

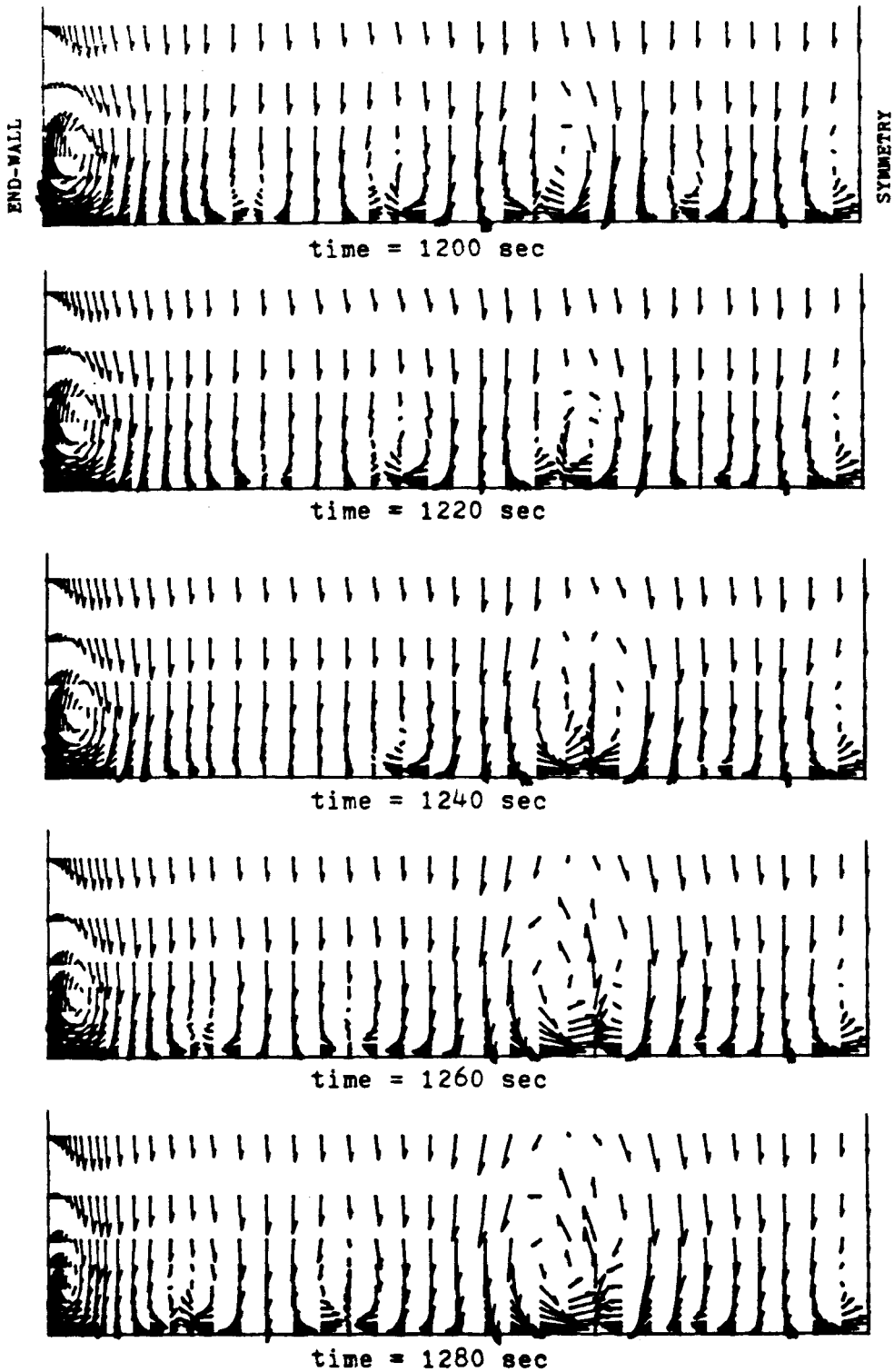

Figure 17. Temporal variation of TG vortices on a plane 35 mm from downstream wall

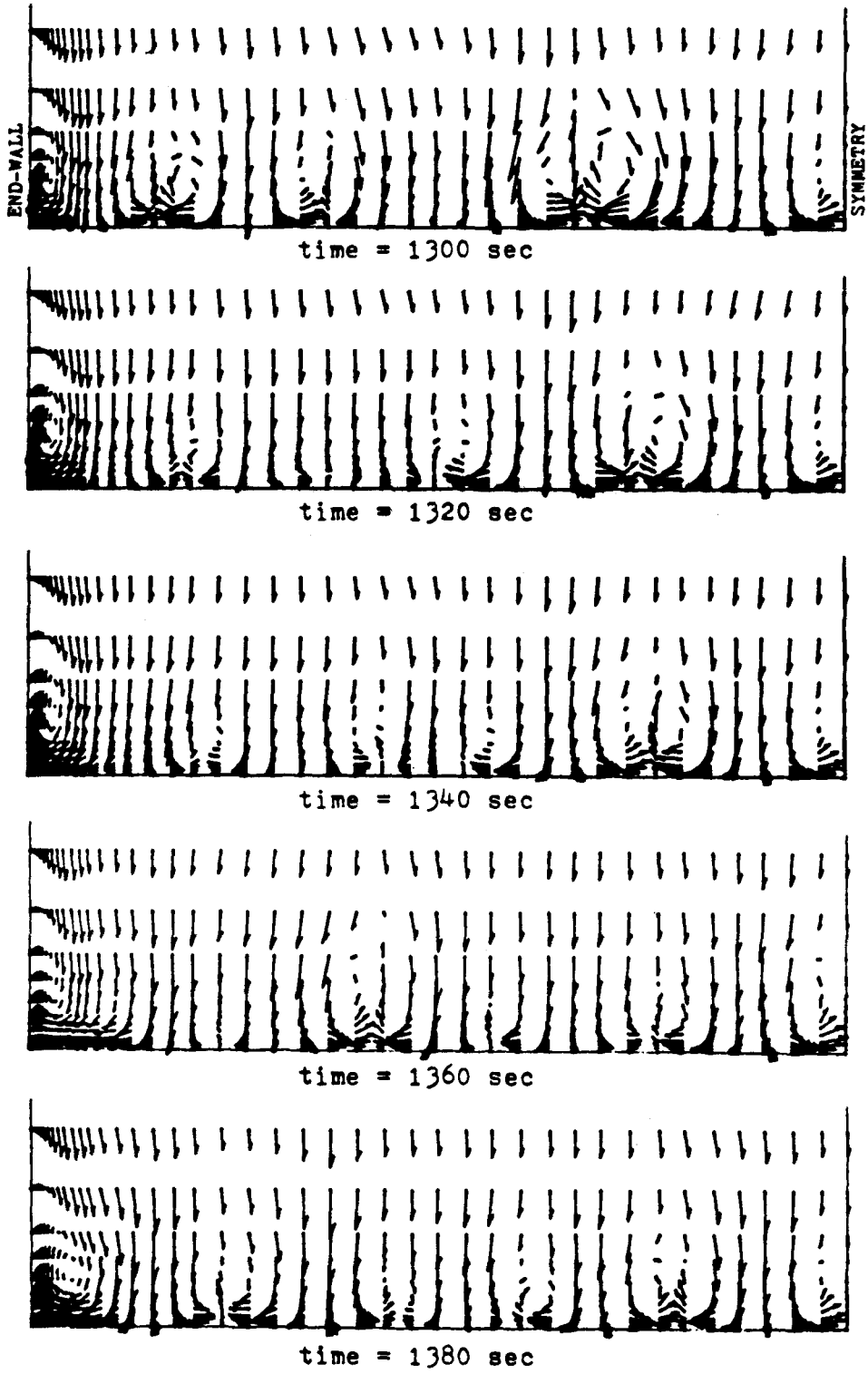

Figure 17. (continued)

scale of about 140 s. A small TG pair has a wavelength of 30 mm and a time scale of about 40 s. Unfortunately no definitive relationship between time and length scales was obtainable from this information. The complex interdependency of each pair on the other pairs and the EWCE precludes such an analysis.

Figure 18 further highlights this interdependency of structures by recording the spanwise variation of normalized vertical velocity at five different times during the 3 min sample interval. These velocities were recorded on a horizontal line 9 mm above the cavity bottom and on the 35 mm plane of Figure 17. The crests of this wave-like distribution represent upflow regions, while the troughs are regions of downflow. This spanwise distribution has been experimentally measured in curved surface boundary layer flow by Meroney and Bradshaw[34] and Winoto and Crane.[31] The end-wall is at $z/B=0{\cdot}0$ and the symmetry plane at $z/B=1{\cdot}50$.

Figures 17 and 18 clearly show that the EWCE size and strength are time-dependent and this variation is related in some degree to the size and strength of the largest TG pair recorded here. As this TG pair grows, the EWCE shrinks, and then the process is reversed. In addition, the number of distinct TG pairs responds to this variation in size of the EWCE and large TG pair by varying from three to four, with smaller vortex pairs disappearing for short periods of time.

The dynamics of a single TG pair is also complex. Focusing again on the large TG pair in Figures 17 and 18, it is observed that the pair oscillates internally. That is, over a 40–50 s interval, one member of the pair is larger and stronger than the other member. Then the process reverses and the other member dominates for approximately the same period. This oscillation is characteristic of Wortmann's[30] description of the secondary instability of Görtler vortices. Due to this internal oscillation of each TG pair and the interdependency of each structure on the others, no well defined global periodic time scale exists. But, during the 3 min time interval recorded in Figures 17 and 18, all the relevant phenomena are described. The anomalous occurrence of the stationary TG vortex at the symmetry plane is also recorded in these figures.

5.3. *Statistics of the flow*

The vertical velocity auto-spectrum or spectral density function is computed at three locations in the cavity, namely at a point between successive TG vortex pairs and at two points influenced by TG vortex motions. The time series at each location consists of 190 points spaced 1 s apart; thus the Nyquist frequency is 0·5 Hz. These spectra are computed by either the standard covariance method (Blackman–Tukey method) or by a fast Fourier transform (FFT) method (Cooley, Lewis and Welch method). In the FFT method only 128 points were used because the radix 2 method employed requires the length of the data set to be a whole exponent for the power of two. Because of its poorer resolution, the FFT method was used only to verify the standard covariance method results. The bandwidth resolution for the standard covariance method is dependent on the number of lags, and the number of lags was varied in order to resolve the pertinent spectral attributes. Figure 19 records the normalized auto-spectral density function for the vertical velocity at the three locations described above. The auto-spectral density function is normalized by the first covariance or sample variance $\langle u^2 \rangle$.

The first observation from Figure 19 is that the peaks of all profiles occur at approximately the same frequency. This frequency of approximately 0·007 Hz (a period of 150 s) is associated with the largest wavelengths of the cavity flow, i.e. with the primary vortex. The length scale of this vortex is equivalent to the cavity width of 150 mm (a wave number of $0{\cdot}04\ \text{mm}^{-1}$). The wave number K and frequency f are related by the relationship $K=2\pi f/U$, where U is the local characteristic velocity of the flow.[35] Thus the associated primary vortex vertical velocity in these regions of the flow can be computed and is approximately 1 to $1{\cdot}5\ \text{mm s}^{-1}$ (depending on the location).

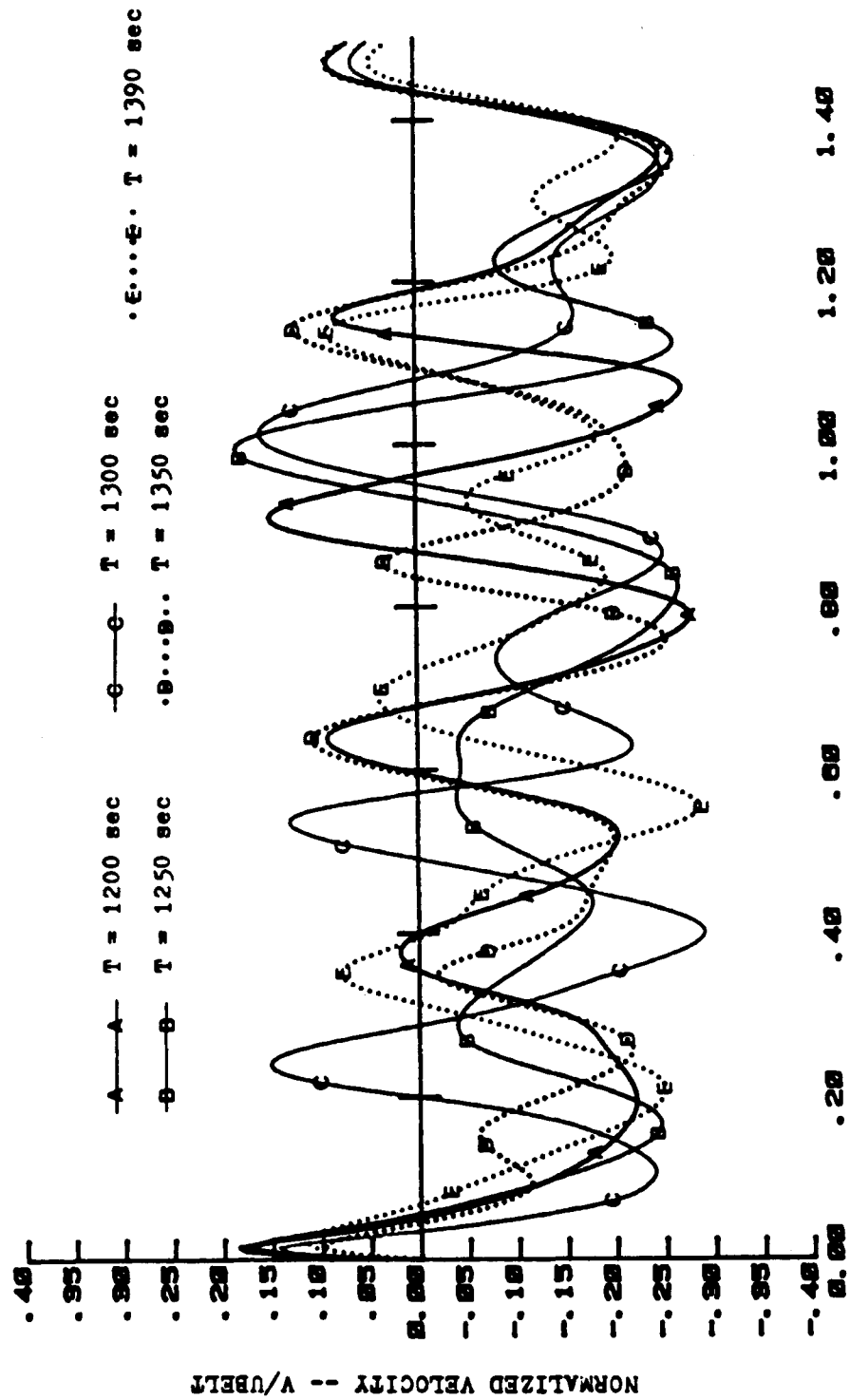

Figure 18. Temporal and spanwise variation of normalized vertical velocity

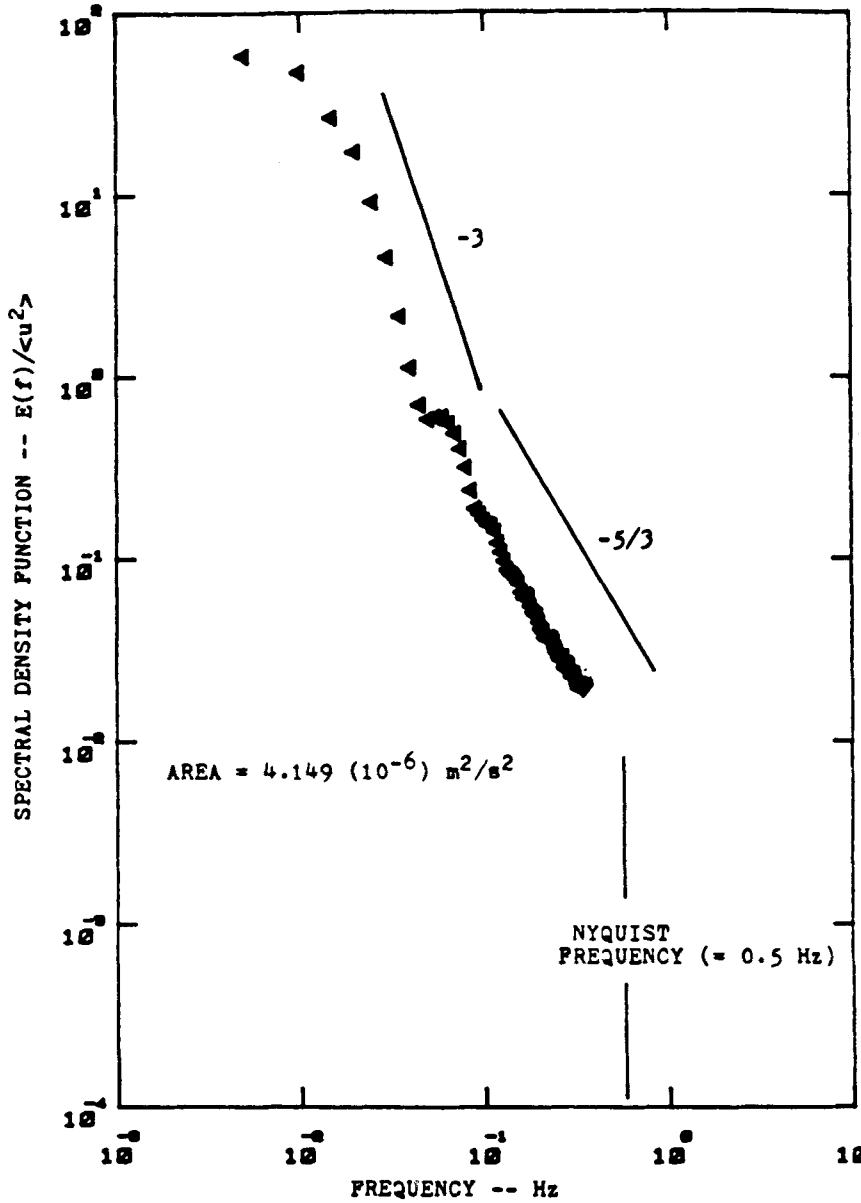

Figure 19(a) Auto-spectrum at a point 35 mm from downstream wall, 10 mm from cavity bottom and 180 mm from end-wall. Region of flow influenced by an intermittent TG vortex pair

Based on the cavity width, the peak frequency and the Nyquist frequency, the minimum resolved wavelength in Figure 19 could be approximately 3 mm (wave number = 2·1 mm^{-1}). This wavelength is smaller than the grid spacing for the majority of the discretized domain. The relevant minimum wavelength for a numerical computation is the $2\Delta x$ wave. This wavelength corresponds to approximately 13 mm for the grid used here. Therefore, based on this wavelength

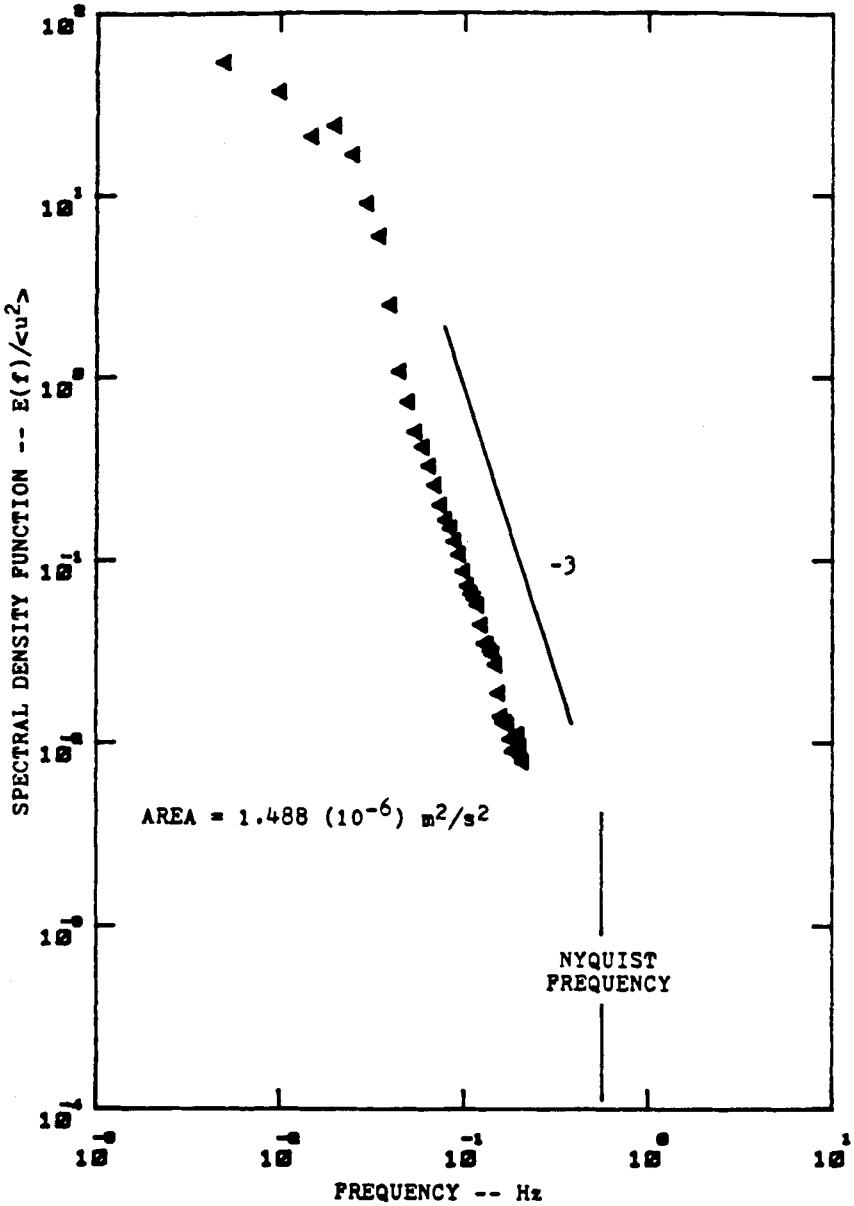

Figure 19(b). Auto-spectrum at a point 35 mm from downstream wall, 10 mm from bottom plate and 135 mm from end-wall. Region of flow influenced by large TG vortex pair

and a characteristic velocity of 1·5 mm s^{-1}, the maximum resolved frequency is approximately 0·11 Hz. The plots in Figure 19 are truncated at this value.

The second observation in Figure 19 is that the spectra associated with regions influenced by TG vortices (Figures 19(a) and (b)) possess greater amounts of energy (described by the area under the spectral curves) than those regions not influenced by TG vortices (Figure 19(c)).

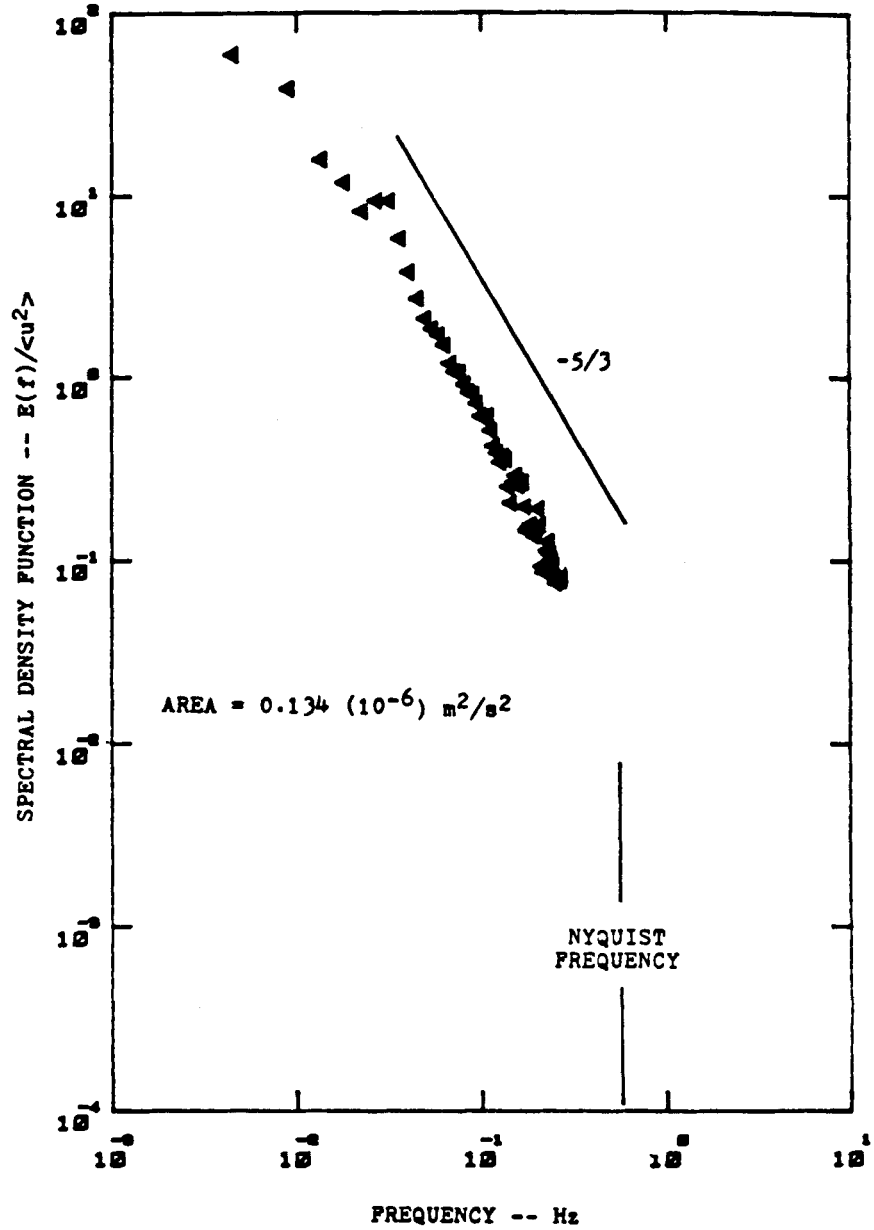

Figure 19(c). Auto-spectrum at a point 35 mm from downstream wall, 10 mm from bottom plate and 195 mm from end-wall. Region of flow not influenced by TG vortices

The third observation is that in regions of the flow dominated by TG vortices the spectra have a frequency range with a -3 slope. A -3 slope is indicative of two-dimensional turbulent flow or flows in a non-equilibrium or accelerated state.[36] Therefore in these regions of the flow the vertical velocity kinetic energy may be contained in two-dimensional-like structures, e.g. TG vortices. In Figure 19(a) a distinct two-slope spectrum is displayed. At this location TG vortices

are transient and disappear for short time intervals. The -3 slope is likely associated with times when TG vortices are present and the $-5/3$ slope (descriptive of three-dimensional turbulent flow or flows in a state of equilibrium) when they are not present. The spectrum in Figure 19(b) is for a point located in a persistent TG pair which exists during the entire sample period. Therefore the spectrum is dominated by a -3 slope.

For a point consistently between TG vortex pairs (Figure 19(c)) the spectrum is dominated by only a $-5/3$ slope. This is again consistent with previous observations, in that no structures are present to organize motions in a two-dimensional manner.

Although this flow is generally not turbulent, it is highly unsteady and may possess limited regions of turbulence. Therefore in these regions energy will be distributed among a range of frequencies and length scales as displayed in Figure 19. In general, one may conclude from this spectral analysis that TG vortices organize the low- to moderate-frequency (moderate wavelength) components of the flow into two-dimensional structures. Outside the domain of influence of TG vortices, the flow responds with fully three-dimensional fluctuations characterized by a $-5/3$ spectral slope.

6. CONCLUSIONS

The dominant physical phenomena in a constant-density-fluid, moderate-Re, three-dimensional cavity flow are the TG vortices. These simulations were the first to reproduce the experimentally observed TG vortex phenomenon in a cavity and to reproduce their consistent physical development. In general, the TG vortex phenomenon is intimately coupled with the primary recirculating flow and the effects of end-wall viscous damping, which results in a pressure-driven secondary flow. In agreement with the physical experiment, the TG vortices which develop in a 150 mm by 150 mm by 450 mm cavity at $Re = 3200$ possess wavelengths in the range 30–50 mm and time scales of 40–140 s.

The influence of TG vortices on the spectral characteristics of the flow has been investigated for the first time. In general, TG vortex regions possess high energy and have spectral slopes indicative of two-dimensional flow or flow in a non-equilibrium or accelerated state. In regions of the flow where TG vortices are absent, the flow possesses less energy and reverts to a three-dimensional spectral structure, indicative of flow in a state of equilibrium.

ACKNOWLEDGEMENTS

The authors wish to thank Dr. Angelos Findikakis, Bechtel Civil & Minerals, Inc., for his counsel during the progress of this work. The review of the manuscript by Dr. Robert Bass, SwRI, is also appreciated. This work was performed primarily in the Environmental Fluid Mechanics Laboratory at Stanford and supported there by the Division of Engineering, Mathematical and Geosciences, Office of Basic Energy Sciences, Department of Energy, through grant DOE-FG03-84ER13240, and by the Hydraulics and Fluid Mechanics Program, National Science Foundation, through Grant MSM-83-12061. The majority of the computations were carried out at the IBM Palo Alto Scientific Center under a Research Support Program Agreement with RLS.

REFERENCES

1. W. Rodi, 'Turbulence models and their application in hydraulics—a state of the art review', IAHR, Delft, 1980.
2. W. Rodi, 'Examples of turbulence—model applications', in *Proc. Ecole d'Ete d'Analyse Numerique—Modelization Numerique de la Turbulence*, Clamart, France, 1982.
3. G. De Vahl Davis and G. D. Mallinson, 'An evaluation of upwind and central difference approximations by a study of recirculating flow', *Comput. Fluids*, **4**, 29–43 (1976).
4. S. Tuann and M. D. Olson, 'Review of computing methods for recirculating flows', *J. Comput. Phys.*, **29**, 1–19 (1978).

5. H. D. Thompson, B. W. Webb and J. D. Hoffman, 'The cell Reynolds number myth', *Int. j. numer. methods fluids*, **5**, 305–310 (1985).
6. S. V. Patankar, *Numerical Heat Transfer and Fluid Flow*, Hemisphere, New York, 1980.
7. U. Ghia, K. N. Ghia and C. T. Shin, 'Solution of incompressible Navier–Stokes equations by coupled strongly implicit multi-grid methods', *Symp. on Multi-Grid Methods*, NASA–Ames Research Center, Moffett Field, CA, October 1981.
8. C. J. Freitas, 'Nonlinear transient phenomena in a three-dimensional cavity flow: a numerical investigation', *Ph.D. Dissertation*, Department of Civil Engineering, Stanford University, Stanford, CA, 1986.
9. J. R. Koseff and R. L. Street, 'Visualization studies of a shear driven three-dimensional recirculating flow', *J. Fluids Eng.*, **106**, 21–29 (1984).
10. J. R. Koseff and R. L. Street, 'The lid-driven cavity flow: a synthesis of qualitative and quantitative observations', *J. Fluids Eng.*, **106**, 390–398 (1984).
11. J. R. Koseff, 'Momentum transfer in a complex recirculating flow', *Ph.D. Dissertation*, Department of Civil Engineering, Stanford University, Stanford, CA, 1983.
12. C. J. Freitas, A. N. Findikakis and R. L. Street, 'The physics of a three-dimensional cavity flow', *Proc. Fourth Int. Conf. on Numerical Methods in Laminar and Turbulent Flow*, University of Wales, Swansea, 9–12 July 1985, pp. 503–514.
13. C. J. Freitas, R. L. Street, A. N. Findikakis and J. R. Koseff, 'Numerical simulation of three-dimensional flow in a cavity', *Int. j. numer. methods fluids*, **5**, 561–575 (1985).
14. J. R. Koseff, R. L. Street, P. M. Gresho, C. D. Upson, J. A. C. Humphrey and W.-M. To, 'A three-dimensional lid-driven cavity flow: experiment and simulation', *Proc. Third Int. Conf. on Numerical Methods in Laminar and Turbulent Flow*, Seattle, WA, August 1983, pp. 564–581.
15. P. LeQuere, J. A. C. Humphrey and F. S. Sherman, 'Numerical calculation of thermally driven two-dimensional unsteady laminar flow in cavities of rectangular cross section', *Numer. Heat Transfer*, **4**, 249–283 (1981).
16. A. D. Gosman and W. M. Pun, 'Lecture notes for course entitled calculation of recirculating flows', *No. HTS/74/2*, Imperial College, London, 1974.
17. S. V. Patankar and D. B. Spalding, 'A calculation procedure for heat, mass, and momentum transfer in three-dimensional parabolic flows', *Int. J. Heat Mass Transfer*, **15**, 1787–1806 (1972).
18. B. P. Leonard, 'A stable and accurate convective modeling procedure based on quadratic upstream interpolation', *Comput. Methods Appl. Mech. Eng.*, **19**, 59–98 (1979).
19. T. Han, J. A. C. Humphrey and B. E. Launder, 'A comparison of HYBRID and quadratic-upstream differencing in high Reynolds number elliptic flows', *Comput. Methods Appl. Mech. Eng.*, **29**, 81–95 (1981).
20. A. Pollard and A. L. W. Siu, 'The calculation of some laminar flows using various discretization schemes', *Comput. Methods Appl. Mech. Eng.*, **35**, 293–313 (1982).
21. M. A. Leschziner, 'Practical evaluation of three finite-difference schemes for the computation of steady state recirculating flows', *Comput. Methods Appl. Mech. Eng.*, **23**, 293–312 (1980).
22. S. Paolucci and D. R. Chenoweth, 'Stability of the explicit finite difference transport equation', *J. Comput. Phys.* **47**, 489–496 (1982).
23. A. O. Demuren, 'Computation of three-dimensional turbulent jets in cross flow', *Proc. Int. Conf. on Computational Methods and Experimental Measurements*, Washington, DC, 1982, pp. 296–313.
24. M. A. Leschziner and W. Rodi, 'Calculation of annular and twin parallel jets using various discretization schemes and turbulence model variations', *J. Fluids Eng.*, **103**, 352–360 (1981).
25. J. H. Ferziger, 'Higher-level simulations of turbulent flows', *Report No. TF-16*, Department of Mechanical Engineering, Stanford University, Stanford, CA, 1981.
26. H. Görtler and H. Witting, in Görtler (ed.), *Boundary Layer Research*, Springer-Verlag, Berlin, 1958.
27. H. Görtler, 'Über eine dreidimensionale Instabilität laminarer Grenzschichten an konkaven Wanden', *Nachr. Wiss. Ges. Göttingen Math.-Phys.*, **K1**, 1–26 (1940).
28. A. M. O. Smith, 'On the growth of Taylor–Görtler vortices along highly concave walls', *Q. Appl. Math.*, **13**, 233–262 (1955).
29. T. Herbert, *Higher Eigenstates of Görtler Vortices*, in Recent Developments in Theoretical and Experimental Fluid Mechanics, Compressible and Incompressible Flows, U. Muller, K. G. Roesner and B. Schmidt (eds), Springer–Verlag, Berlin, 1979, pp. 322–330.
30. F. X. Wortmann, 'Visualization of transition', *J. Fluid Mech.*, **38** (Part 3), 473–480 (1969).
31. S. H. Winoto and R. I. Crane, 'Vortex structure in laminar boundary layers on a concave wall', *Int. J. Heat Fluid Flow*, **2** (4), 221–231 (1980).
32. J. Kim and P. Moin, 'Application of a fractional-step method to incompressible Navier–Stokes equations', *J. Comput. Phys.*, **59**, 308–323 (1985).
33. Y. Aihara, 'Nonlinear analysis of Görtler vortices', *Phys. Fluids*, **19** (11), 1655–1660 (1976).
34. R. N. Meroney and P. Bradshaw, 'Turbulent boundary-layer growth over a longitudinally curved surface', *AIAA J.*, **13** (11), 1448–1453 (1975).
35. J. O. Hinze, *Turbulence*, McGraw-Hill, New York, 1975.
36. H. B. Fischer (ed.), *Transport Models for Inland and Coastal Waters*, Proceedings of Symposium on Predictive Ability, Academic Press, London, 1981.